

Structure, topology, rings, and vibrational and electronic properties of $\text{Ge}_x\text{Se}_{1-x}$ glasses across the rigidity transition: A numerical study

M. Micoulaut,^{1,*} A. Kachmar,¹ M. Bauchy,¹ S. Le Roux,² C. Massobrio,² and M. Boero²

¹*Laboratoire de Physique Théorique de la Matière Condensée, Université Pierre et Marie Curie, 4 Place Jussieu, F-75252 Paris Cedex 05, France*

²*Institut de Physique et de Chimie des Matériaux de Strasbourg, 23 rue du Loess, Boîte Postale 43, F-67034 Strasbourg Cedex 2, France*

(Received 27 May 2013; revised manuscript received 12 July 2013; published 23 August 2013)

The structural, electronic, and vibrational properties of glassy $\text{Ge}_x\text{Se}_{1-x}$ are studied using density-functional-based molecular dynamics. The focus is on four compositions ($x = 10\%, 20\%, 25\%, 33\%$) spanning the rigidity transitions and representing typical compositions of flexible, intermediate, and stressed rigid systems. We investigate structural properties including structure factors, pair distribution functions, angular distributions, coordination numbers, and neighbor distributions and compare our results with experimental findings, when available. Most noticeable is the excellent agreement found in the reproduction of the structure in real and reciprocal space which allows tracking the effect of Ge composition on the structure. Ring statistics and ring correlations are examined and followed across the rigidity transition, and the details of typical small rings show a much more complex picture than established previously. A comparison is made with simple bond models and their validity is discussed. Topological constraint analysis is performed and shows that the onset of rigidity changes substantially the angular motion inside the Ge tetrahedra, which displays increased soft bending motions in the stressed rigid phase. We then investigate the vibrational properties via the vibrational density of states and the dielectric function (infrared absorption), and discuss them with respect to experimental findings. Finally, the electronic properties are computed and show an excellent agreement with respect to previous first-principles simulations and to experiments.

DOI: [10.1103/PhysRevB.88.054203](https://doi.org/10.1103/PhysRevB.88.054203)

PACS number(s): 61.43.Fs, 61.25.Em, 61.20.Ja

I. INTRODUCTION

Germanium selenides $\text{Ge}_x\text{Se}_{1-x}$ not only form an interesting class of glasses or starting materials used for optoelectronic applications,^{1–8} they also represent archetypal covalently bonded networks⁹ which progressively stiffen¹⁰ as their mean coordination number $\bar{r} = 2 + 2x$ increases. They can undergo light-induced changes^{11–14} or even spectacular photocontraction effects,^{15–17} and also electrical switching phenomena,¹⁸ so that a large amount of research has been conducted to characterize the basics of physicochemical properties, and the potentialities of promising applications.

A. Rigidity and structure of Ge-Se glasses: A deceitful simplicity

For a long period, the observed compositional trends have been understood from concepts which are directly derived from the Maxwell elasticity theory for macroscopic structures.^{19,20} In fact, from a mechanical viewpoint, the stretching and bending interactions which constrain the network at a molecular level²¹ can be identified with mechanical constraints n_c which are compared to the available degrees of freedom n_d .^{22–25} This analysis shows that glasses with a low connectedness containing a large fraction of twofold-coordinated chalcogens (Se) are flexible because $n_c < n_d$, whereas a network consisting of a large amount of Ge atoms is intrinsically rigid. At the exact boundary $n_c = n_d$ corresponding to the isostatic stability criterion defined by Maxwell, a flexible-to-rigid transition has been predicted, verified from various observed anomalies in materials properties.^{26–31}

Given the elastic nature of the predicted threshold^{22,23} and the connection with optimal glass formation,²¹ a certain number of experimental studies have focused either on the enthalpic properties at the glass transition^{32–34} including under aging,^{35,36} or on elastic properties,^{37–39} sound velocity,^{40,41} and viscosity.^{42–44}

This traditional picture for the onset of rigidity in these glasses has been challenged because evidence^{45–49} for the absence of a single transition or threshold has been reported, defining for $\text{Ge}_x\text{Se}_{1-x}$ glasses an intervening region (an intermediate phase, IP) from $x_c(1) = 20\%$ to $x_c(2) = 26\%$ Ge between the flexible and the stressed rigid phase (gray zone in Fig. 1). In the IP, glasses display some remarkable properties such as weak aging^{52,53} or internal stress,⁵⁴ and space-filling tendencies^{55,56} (see Fig. 1, right axis). These properties appear to be generic as they have also been observed in other glasses such as binary or multicomponent oxides,^{48,57–62} or even in complex materials⁶³ including proteins.^{64,65} The emergence of this IP and the discussion about its origin have not been without controversy, as many studies have debated on the validity of one of the key measurements, a nonreversing enthalpy ΔH_{nr} measured at the glass transition (Fig. 1), while unfortunately overlooking other obvious experimental signatures.^{45–47,52–54,66,67} At this stage of knowledge, however, it appears that the IP is highly sensitive to the homogeneity^{50,68,69} or dryness⁷⁰ of the samples, so that a careless synthesis may lead to incorrect results or even to wrong statements, especially regarding aging.^{71,72} These phenomena have been fairly well described by modifying previous theories of the rigidity transition.^{24,25} Such phenomenological models have shown that the occurrence of the IP results from

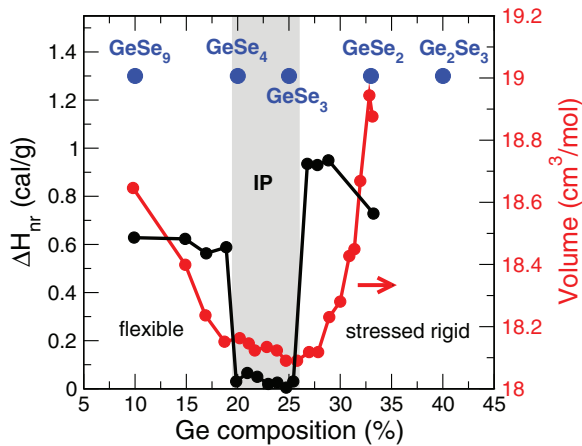


FIG. 1. (Color online) Anomalous behavior of thermal quantities of $\text{Ge}_x\text{Se}_{1-x}$ glasses across the intermediate phase (taken from Ref. 50): Nonreversible heat flow $\Delta H_{nr}(x)$ (black curve) showing a deep minimum for carefully homogenized glasses. Right axis: molar volume (red curve). The systems investigated by first-principles molecular dynamics (FPMD) are shown in blue: GeSe_9 , GeSe_4 , GeSe_3 , and GeSe_2 . Results (Ref. 51) from amorphous Ge_2Se_3 are also discussed throughout the paper.

a self-organization^{24–26,73} or adaptation^{74,75} of the network which accommodates stress for $x > x_c(1)$ in rigid networks by accumulating isostatic regions and delaying percolation of stressed rigidity up to a certain point $x_c(2)$ identified with a stress transition.

Regarding structure, one naturally expects that experiments and molecular simulations will provide an interesting perspective for the detection of a signature of rigidity onset at the atomic scale. Experimentally, various measurements have been used to characterize the structural changes induced by the increase of Ge content in $\text{Ge}_x\text{Se}_{1-x}$ glasses, in connection with rigidity transitions: neutrons,^{76–84} x rays,^{85–90} extended x-ray absorption fine structure (EXAFS),^{48,91–94} Raman spectroscopy,^{45,49,50,68,69,95–97} inelastic neutron scattering,^{27,98–100} anomalous x-ray spectroscopy,^{101,102} Mössbauer spectroscopy,^{9,10,103,104} and nuclear magnetic resonance (NMR).^{105–108}

In parallel, there has been a continuous effort in simulating the structure from molecular simulations, especially on the stoichiometric GeSe_2 compound. One major challenge regarding this system and related Ge-Se alloys is that they contain bonding defects.^{79–83,109,110} They also display chemical bonding between ionic and covalent character, while also showing semimetallic behavior under pressure¹¹¹ or with temperature.¹¹² Therefore, simple attempts using either reverse Monte Carlo (RMC) simulations^{102,113–115} or classical molecular dynamics^{116–120} (including the computation of the vibrational spectra¹²¹) have failed in reproducing the details of the chemical bonding of GeSe_2 glasses, most of these computational efforts having been accomplished at a time when there was only indirect evidence of homopolar Ge-Ge and Se-Se bonds,^{103,104} i.e., before the publication of the full partial structure factor analysis revealing in a neat way these bonding types.^{109,110} More recent contributions using either three-body force fields^{122,123} or polarizable ion models^{124,125}

still do not reproduce accurately the structure of GeSe_2 . One has therefore to rely on first-principles molecular dynamics (FPMD), which can account for all the electronic features of the chemical bonding and its change with temperature or composition while also allowing for the computation of properties inaccessible from classical molecular dynamics. This is the purpose of the present paper.

B. General purpose

In the present contribution, we investigate the structural, electronic, and vibrational properties of $\text{Ge}_x\text{Se}_{1-x}$ for four selected compositions spanning the flexible, intermediate, and stressed rigid phases⁵⁰ of this system, i.e., we focus on the particular systems GeSe_9 , GeSe_4 , GeSe_3 , and GeSe_2 (Fig. 1). We also use results from a recently reported study⁵¹ of glassy Ge_2Se_3 using the same simulation procedure (see below).

Previous work using approximate *ab initio* methods has been reported on several compositions of the Ge-Se system.^{126–129} Calculations have also been performed on isolated clusters.^{130–132} In the present case, the chosen electronic scheme of density functional theory (DFT) using plane-wave basis sets has been established after a series of methodological investigations on both liquid and glassy Ge-Se alloys.^{133–136} First, a generalized gradient approximation (GGA) has been used for the exchange-correlation energy. It goes beyond the local density approximation (LDA) and improves substantially¹³⁷ the description of both short- and intermediate-range order in liquid GeSe_2 . Second, an alternative exchange-correlation functional has been tested¹³⁸ (with respect to Ref. 137), derived after Becke (B) for the exchange energy¹³⁹ and Lee, Yang, and Parr (LYP) for the correlation energy.¹⁴⁰ An increase of the tetrahedral geometry has been found,¹³⁸ together with a reduction of the metallic character of the bonding, thus providing an increased accuracy with respect to experimental measurements on structure in real and reciprocal space for both liquid and glassy GeSe_2 (Refs. 138, 141, and 142) and related compounds,¹⁴³ and also in vibrational¹⁴⁴ and NMR properties.¹⁴⁵ These series of investigations validate the GGA-BLYP scheme as the optimal electronic model for the simulation of germanium selenides.

Here, various structural properties in glassy Ge-Se are computed, and when compared to experimental measurements, these show very good agreement, especially for the structure factors in reciprocal space. In real space, our results show that the increase of Ge leads to important changes in structure which are manifest by the occurrence of homopolar Ge-Ge bonding in the intermediate phase while the compounds show also nonmonotonic variations in ring structure and ring connectivity. We then also analyze the electronic (electronic density of states) and vibrational properties of these glasses by computing the vibrational density of states (VDOS) and the dielectric function, whose imaginary part is compared to experimental results from infrared absorption. Taken together, these results provide a systematic plane-wave DFT study of compositions across the stiffness transitions. Effects of the flexible-to-rigid transition are detected from the angular motion of the germanium which softens some bond-bending constraints as the system becomes stressed rigid.

The article is organized as follows. Section II describes the electronic model used and the details of the FPMD simulations of $\text{Ge}_x\text{Se}_{1-x}$. Section III gives the results of our simulations in reciprocal space by comparing the calculation of the Bhatia-Thornton partial structure factors at different compositions to available experimental data obtained from neutron diffraction. Section IV provides pair distribution functions, bond angle distributions, coordination number distributions, and ring statistics. In Sec. V, we compare our findings regarding the bonding and ring statistics with simple models reported in the literature, and discuss their validity. We also compute bonding constraints and provide an atomic-scale picture of the stiffening of the network structure as the Ge content is increased. Section VI presents the results on the electronic properties and their evolution with composition, while Sec. VII presents the vibrational properties of the glasses consisting of the VDOS and the dielectric function. Finally Sec. VIII summarizes our findings, and brings up some conclusions and perspectives.

II. COMPUTATIONAL DETAILS

Simulations on four compositions $\text{Ge}_x\text{Se}_{1-x}$ have been performed at constant volume on systems consisting of $N = 120$ atoms (with $N_{\text{Ge}} = xN$ and $N_{\text{Se}} = (1-x)N$, e.g., 30 Ge atoms and 90 Se atoms for GeSe_3). A periodically repeated cubic cell was used. The sizes used allowed the experimental density of the glass¹⁴⁶ to be recovered with pressures that do not exceed 0.5 GPa. The electronic structure has been described within density functional theory and evolved self-consistently during the motion.¹⁴⁷ We have adopted here a generalized gradient approximation using the exchange energy obtained by Becke¹³⁹ and the correlation energy according to Lee, Yang, and Parr.¹⁴⁰ Valence electrons were treated explicitly, in conjunction with norm-conserving pseudopotentials of the Trouiller-Martins type to account for core-valence interactions. The wave functions were expanded at the Γ point of the supercell on a plane-wave basis set with an energy cutoff $E_c = 20$ Ry. A fictitious electron mass of 200 a.u. was used for the first-principles molecular dynamics approach, and the time step was set to $\Delta t = 0.12$ fs to integrate the equations of motion. Temperature control was implemented for both the ionic and electronic degrees of freedom by using Nosé-Hoover thermostats. Additional details on the simulation can be found in Ref. 138.

The initial coordinates of the 120-atom system were obtained from previous simulations on stoichiometric GeSe_2 .¹³⁸ Ge atoms were randomly replaced by Se atoms, prior to an initial simulation of 25 ps at 2000 K in order to lose memory of the initial configuration. Additional runs each of 25 ps were performed at temperatures of 1373 and 1050 K. At the latter temperature, four independent configurations separated by time intervals of 5 ps were chosen and served as starting configurations of four independent quenches to the glassy state, performed at an average cooling rate of ≈ 10 K/ps. Finally, for each composition statistical averages were performed at 300 K over the four quenched samples accumulated over a time interval of 84 ps. We then calculate various quantities for the GeSe_9 , GeSe_4 , GeSe_3 , and GeSe_2 systems, and follow their trends with composition. Results

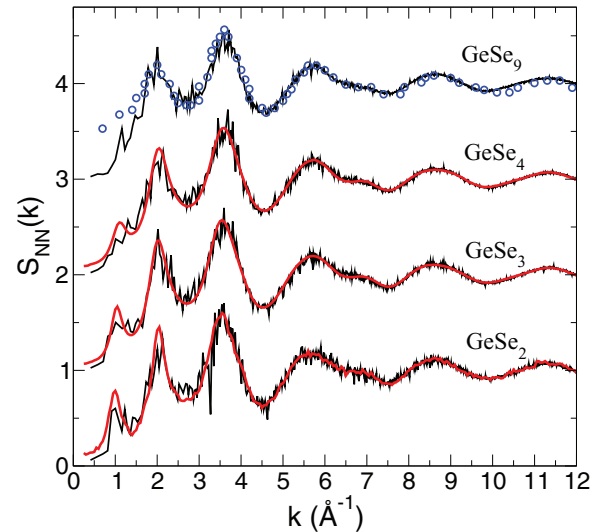


FIG. 2. (Color online) Computed Bhatia-Thornton number-number structure factor $S_{\text{NN}}(k)$ as a function of composition x in $\text{Ge}_x\text{Se}_{1-x}$ glasses, compared to results from neutron diffraction for GeSe_2 , GeSe_3 , and GeSe_4 (red, Ref. 83) and GeSe_9 (blue circles, Ref. 78, total structure factor).

from a recently investigated Ge_2Se_3 glass⁵¹ are also considered during the discussion.

III. RECIPROCAL-SPACE PROPERTIES

In Fig. 2, we display the calculated Bhatia-Thornton¹⁴⁸ number-number (NN) structure factor $S_{\text{NN}}(k)$ for the four selected compositions, and compare them with available experimental results obtained from neutron diffraction (red curves). This partial structure factor measures correlations between scattering centers independently of their chemical nature,^{110,148,149} and usually represents a very good approximation of the total structure factor $S_T(k)$ defined by

$$S_T(k) = S_{\text{NN}}(k) + A [S_{\text{CC}}(k)/c_{\text{Ge}} c_{\text{Se}} - 1] + B S_{\text{NC}}(k), \quad (1)$$

where $A = x(1-x)\Delta b^2/\langle b \rangle^2$, $B = 2\Delta b/\langle b \rangle$, $\Delta b = b_{\text{Ge}} - b_{\text{Se}}$, $\langle b \rangle = c_{\text{Ge}}b_{\text{Ge}} + c_{\text{Se}}b_{\text{Se}} = xb_{\text{Ge}} + (1-x)b_{\text{Se}}$, and where the coherent scattering lengths of the chemical species are given by $b_{\text{Ge}} = 8.185$ fm and $b_{\text{Se}} = 7.97$ fm.¹⁴⁸ In fact, the coefficients A and B are found to vary from $A = 6.5 \times 10^{-5}$ to 1.6×10^{-4} , and from $B = 0.054$ to 0.053 , respectively, when the composition is changed from $x = 10\%$ (GeSe_9) to 33% (GeSe_2). This leads to $|S_T(k) - S_{\text{NN}}(k)| < 0.015$ for nearly all compositions, i.e., one can consider that $S_T(k) \simeq S_{\text{NN}}(k)$, which results directly from the fact that $b_{\text{Ge}} \simeq b_{\text{Se}}$. These structure factors $S_{\text{NN}}(k)$, $S_{\text{CC}}(k)$, and $S_{\text{NC}}(k)$ can be obtained by linear combinations¹⁴⁸ of the Faber-Ziman structure factors $S_{\text{GeGe}}(k)$, $S_{\text{GeSe}}(k)$, and $S_{\text{SeSe}}(k)$, which are not represented here.

An excellent agreement of the calculated $S_{\text{NN}}(k)$ with the experimental counterpart is found, with all typical features being reproduced over the entire range of wave vectors k : the first sharp diffraction peak (FSDP) at $k \simeq 1$ \AA^{-1} as in experiments,⁸³ the first principal peak (PP1) at $\simeq 2$ \AA^{-1} , and

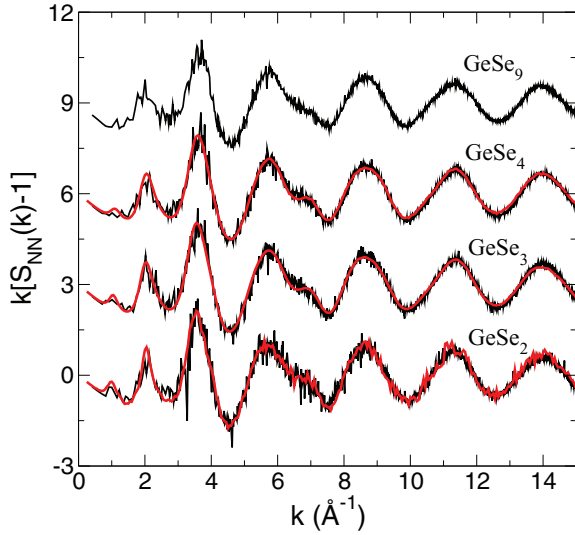


FIG. 3. (Color online) Computed Bhatia-Thornton interference function $I_{NN}(k) = k[S_{NN}(k) - 1]$ as a function of composition x in $\text{Ge}_x\text{Se}_{1-x}$ glasses, compared to results from neutron diffraction (red, Ref. 83).

the second principal peak (PP2) at $\approx 3.6 \text{ \AA}^{-1}$. The high-wave-vector region ($k > 10\text{--}12 \text{ \AA}^{-1}$) is also very well reproduced as shown from the interference function $I_{NN}(k) = k[S_{NN}(k) - 1]$ which blows up the oscillations found at higher k value (Fig. 3). This agreement provides confidence that real-space properties at short distances r ($r \propto 1/k$) should also be reasonably well reproduced. Both principal peaks (PPs) are found to slightly vary with composition, e.g., the PP2 peak shifts from 3.62 \AA^{-1} for GeSe_9 to 3.59 \AA^{-1} for GeSe_2 , while its width Δk_{PP2} (determined from a Lorentzian fit, see Table I) is found to increase with Ge composition, from 1.74 to 2.70 \AA^{-1} . Similar features are found for the other principal peak (PP1), i.e., a redshift of the position k_{PP1} and a reduction of the width Δk_{PP1} leading to a sharper PP1 for the stoichiometric GeSe_2 . One also notes the emergence of a FSDP as the network becomes more and more connected, i.e., for the GeSe_4 composition. The FSDP is indeed nearly absent for the GeSe_9 composition,

TABLE I. Calculated partial structure factor parameters (in \AA^{-1}) extracted from a Lorentzian fit of the main peaks: position k_i and width Δk_i , $i = \{\text{FSDP}, \text{PP1}, \text{PP2}\}$. All of them are given with $\Delta k = \pm 0.01 \text{ \AA}^{-1}$.

$S_{ij}(k)$	System	k_{FSDP}	k_{PP1}	Δk_{PP1}	k_{PP2}	Δk_{PP2}
$S_{NN}(k)$	GeSe_9		2.02	2.16	3.62	1.74
	GeSe_4		2.08	1.83	3.62	1.78
	GeSe_3	1.16	2.10	1.77	3.60	2.20
	GeSe_2	1.14	2.07	1.13	3.59	2.70
$S_{CC}(k)$	GeSe_9		2.16	2.05		
	GeSe_4	1.00	2.09	0.71		
	GeSe_3	0.91	2.08	0.52		
	GeSe_2	1.00	2.09	0.44		
$S_{NC}(k)$	GeSe_9	1.11	1.98	1.36		
	GeSe_4	1.10	2.01	0.78		
	GeSe_3	1.04	2.01	0.65		
	GeSe_2	1.08	2.02	0.49		

and builds up for larger Ge content while also agreeing with the experimental data.⁷⁸

A similar level of agreement is obtained for the two other partial structure factors $S_{CC}(k)$ and $S_{NC}(k)$ involving long-range concentration-concentration and concentration-number correlations.^{83,149} These calculated functions can be only compared to the experimental results of the system GeSe_2 , the only composition for which isotopically substituted neutron scattering measurements (which give access to such partials) have been performed.⁸³ Simulations for the other compositions thus bring additional insight into the network structure. Obvious trends emerge indeed from the represented functions when these are considered as a function of Ge content. For instance, we note that concentration-concentration (CC) fluctuations are nearly absent for the GeSe_9 compound given the weak abundance of Ge atoms. In the high-wave-vector region, it is seen that $S_{CC}(k)$ converges to the limit $c_{\text{Ge}}c_{\text{Se}} = x(1-x) = 0.09$, which directly comes from the definition^{83,148}

$$S_{CC}(k) = c_{\text{Ge}}c_{\text{Se}}[1 + S_{\text{GeGe}}(k) + S_{\text{SeSe}}(k) - 2S_{\text{GeSe}}(k)], \quad (2)$$

where $S_{\text{GeGe}}(k)$, $S_{\text{GeSe}}(k)$, and $S_{\text{SeSe}}(k)$ are the Faber-Ziman structure factors which obey the limit $S_{ij}(k) \rightarrow 1$ for large k . One observes from Fig. 4 that the positive or negative oscillations with respect to the limit $c_{\text{Ge}}c_{\text{Se}}$ have a very low amplitude in GeSe_9 . Since this function $S_{CC}(k)$ provides information about chemical ordering^{149,150} of the Ge and Se species at an intermediate scale, oscillations usually indicate a preference for like (Ge-Ge, Se-Se) or unlike (Ge-Se) correlations. Here, given these small oscillations one can conclude that such correlations are absent, indicating that one has a random mixing of Ge atoms into the base Se-rich network. This is also independently suggested from the glass transition variation, where predictive scaling laws have been established on the basis of a random cross-linking of Ge in Se chain fragments,^{151,152} at variance with network adaptation which occurs at higher Ge composition.²⁴ With increasing Ge content, a peak at 2.10 \AA^{-1} emerges in the function $S_{CC}(k)$

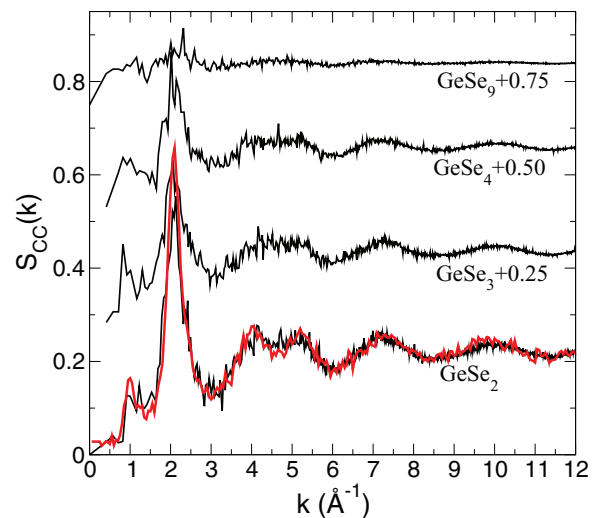


FIG. 4. (Color online) Computed Bhatia-Thornton concentration-concentration structure factor $S_{CC}(k)$ as a function of composition x in $\text{Ge}_x\text{Se}_{1-x}$ glasses, compared to results from neutron diffraction (red, Ref. 83).

and its amplitude grows to become the dominant feature of this partial structure factor for the GeSe_2 composition. One also obtains a FSDP in the region $0.9\text{--}1.0 \text{ \AA}^{-1}$ which does not show any marked changes with Ge composition as manifested by the evolution of the position $k_{\text{FSDP}} \simeq 1 \text{ \AA}^{-1}$ (Table I). The position of the FSDP is usually associated with some repetitive characteristic distance between structural units involving a typical length scale for concentration-concentration correlations of $7.7/k_{\text{FSDP}} = 7.7 \text{ \AA}$.¹⁵³ Similarly, the width of the FSDP is indicative of a coherence length, following the well-known Scherrer equation for microcrystals which relates the width of a Bragg peak with the average size of the microcrystals (for a monocrystal, one has $\Delta k_{\text{FSDP}} \simeq 0$). A coherence length for ordering defined by $\xi_{\text{CC}} = 7.7/\Delta k_{\text{FSDP}}$ can be established,¹⁵³ having used a Lorentzian fit for the FSDP. From the variation of the FSDP in $S_{\text{CC}}(k)$ with x (Fig. 4), one realizes that an important growth of ξ_{CC} takes place between the GeSe_4 ($\xi_{\text{CC}} \simeq 6.3 \text{ \AA}$) and the GeSe_3 ($\xi_{\text{CC}} \simeq 16.0 \text{ \AA}$) compositions. This indicates that in the intervening region (i.e., the IP), important changes in chemical ordering take place at an intermediate length scale, as also revealed by the real-space analysis (see below).

When the Ge content is increased, similar features are found for the number-concentration Bhatia-Thornton function $S_{\text{NC}}(k)$ defined as

$$S_{\text{NC}}(k) = c_{\text{Ge}}c_{\text{Se}}[c_{\text{Ge}}(S_{\text{GeGe}}(k) - S_{\text{GeSe}}(k)) - c_{\text{Se}}(S_{\text{SeSe}}(k) - S_{\text{GeSe}}(k))]. \quad (3)$$

This function focuses on the correlations between scattering centers (number) and occupation by a given Ge or Se species (concentration) in a diffraction experiment.¹⁴⁸ As seen from Eq. (3), it is a measure of how chemical-like species order on length scales typical of a given wave vector k because $S_{\text{NC}}(k)$ goes to zero if $S_{\text{GeGe}}(k) \neq S_{\text{SeSe}}(k)$. In the series of investigated Ge-Se compositions (Fig. 5), a FSDP is obtained at a wave-vector position of about $\simeq 1.1 \text{ \AA}^{-1}$ (Table I) which obviously sharpens with Ge content, similarly to $S_{\text{CC}}(k)$,

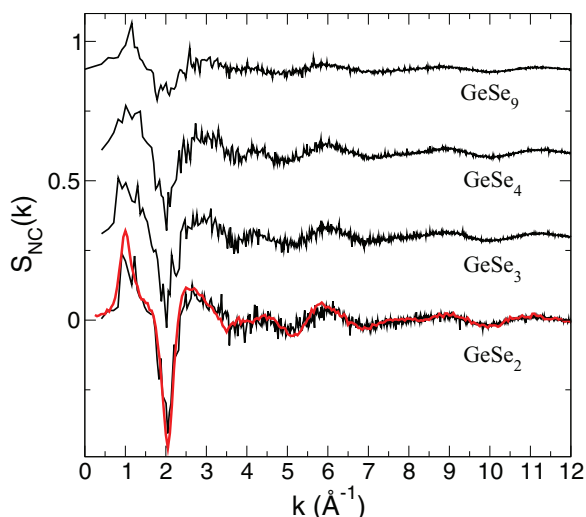


FIG. 5. (Color online) Computed Bhatia-Thornton number-concentration structure factor $S_{\text{NC}}(k)$ as a function of composition x in $\text{Ge}_x\text{Se}_{1-x}$ glasses, compared to results from neutron diffraction (red, Ref. 83).

and also similarly to the principal peak in $S_{\text{NC}}(k)$ found at $1.98\text{--}2.02 \text{ \AA}^{-1}$. A Lorentzian fit of the FSDP shows that $\Delta k_{\text{FSDP}} \simeq 1.96 \text{ \AA}^{-1}$ for GeSe_4 and decreases to 0.8 \AA^{-1} for GeSe_2 , implying an increase by more than a factor of 2 for the corresponding coherence length ξ_{NC} .

To summarize this section, we find an excellent agreement over the entire wave-vector range, and for all compositions, when our computed $S_{ij}(k)$ ($i, j = \text{N, C}$) are compared to experimental results from isotopic substitution diffraction.^{83,110,149} The detail of the partial structure factors shows that most of the peaks (FSDP, PP1, and PP2), while changing moderately in position, sharpen once the Ge content is increased. This underscores the emergence of various coherence lengths ξ_{ij} associated with the increase of connectedness induced by the cross-linking Ge atoms. $S_{\text{NN}}(k)$ probes only the scattering centers, independently of the nature of the chemical species (Ge, Se), and is therefore a measure of how the topology of the network is modified at intermediate length scales. Flexible-to-rigid transitions are by their essence of topological nature because they are revealed by the control parameter of the transition, the mean network coordination number $\bar{r} = 2 + 2x$, which can be directly derived⁸² from the Bhatia-Thornton pair distribution function $g_{\text{NN}}(r)$ [the Fourier transform of $S_{\text{NN}}(k)$]. One might therefore expect that some typical features appear when the characteristic peaks of $S_{\text{NN}}(k)$ are followed with composition across the transition. On the other hand, $S_{\text{CC}}(k)$ provides information about the way these chemical species are distributed throughout the network characterized by $S_{\text{NN}}(k)$. As mentioned above, it provides a measure of the chemical order as the variation of this partial structure factor is directly linked to the product of the concentrations c_{Ge} and c_{Se} of the two species involved [Eq. (2)]. Since the stiffening of the network and the onset of rigidity are tied to the occurrence of more and more stressed rigid Ge-Se-Ge connections, one may also expect that a signature of rigidity transitions manifests in the partial $S_{\text{CC}}(k)$ as well. From our computed partial structure factor, we do not find any evidence for anomalies or thresholds with varying composition, and the parameters characterizing the peaks (Table I) follow only smooth trends although displaying marked changes for the IP compositions (GeSe_4 and GeSe_3). This conclusion is in line with an analysis for various selenides of the FSDP of the total structure factor showing no change⁸⁴ in behavior once the network becomes stressed rigid. However, a detailed analysis of partials in a parent system¹⁵⁴ shows that anomalies and threshold properties manifest indeed at the expected rigidity transition.¹⁵⁵ Concerning the present Ge-Se system, more compositions obviously need to be studied to track within tiny compositional changes the flexible transition and the intermediate phase. This would of course require larger system sizes,¹⁵⁶ and is clearly beyond the scope of the present contribution.

IV. REAL-SPACE PROPERTIES

A. Pair distribution functions

We now turn to real-space properties and follow these with Ge content. Figure 6 shows the computed total pair distribution function for the $\text{Ge}_x\text{Se}_{1-x}$ glasses, compared to available measurements from the literature.^{83,157} It appears that

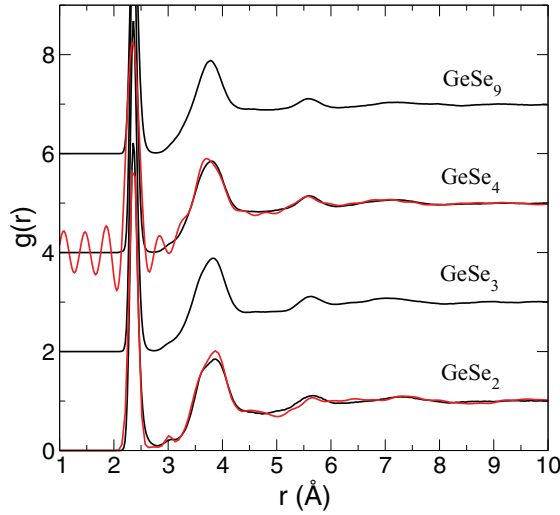


FIG. 6. (Color online) Computed total pair distribution function $g(r)$ for different compositions x in $\text{Ge}_x\text{Se}_{1-x}$ glasses, compared to results (red curves) from neutron diffraction (GeSe_2 , Ref. 83, and GeSe_4 , Ref. 157). The unphysical oscillations at low r in the GeSe_4 compound arise from the the Fourier transform of the experimental structure factor for distances lower than the closest approach between atoms.

the agreement is, again, excellent as all features of the pair distribution function, the main peak at 2.36 Å (experimentally⁸³ 2.35 Å) and secondary peak at 3.85 Å are reproduced with great accuracy, when compared to experiments on GeSe_2 (Ref. 83) and GeSe_4 .¹⁵⁷ The large intensity of the first peak, which mostly arises from the Ge-Se bond distance, actually overwhelms in Ge-rich glasses other contributions due to Ge-Ge and Se-Se correlations in the structure (see also the peak positions in Table II), and which can be investigated from a detailed analysis of the pair distribution functions g_{ij} (Fig. 7). We also report in Table II the corresponding number of neighbors and peak positions $d(X-X^i)$ with $X = \text{Ge}, \text{Se}$ and $i = \text{I}, \text{II}, \text{III}$. The secondary peak at $\simeq 3.85$ Å which does not seem to vary much with composition (Fig. 6) actually results from various contributions which depend strongly on the Ge content, as discussed below.

For the stoichiometric compound GeSe_2 , we find an excellent agreement for all pairs, most features (peak positions and peak widths) being very well reproduced, as are also the peaks reflecting homopolar bondings. Distances found, at $d(\text{Ge}-\text{Ge}^{\text{I}}) = 2.44$ Å in g_{GeGe} and at $d(\text{Se}-\text{Se}^{\text{I}}) = 2.37$ Å in g_{SeSe} , compare very favorably with the experimental estimates of $d(\text{Ge}-\text{Ge}^{\text{I}})_{\text{expt}}$ and $d(\text{Se}-\text{Se}^{\text{I}})_{\text{expt}}$ (see Table II) which have been found to be equal to 2.42 and 2.32 Å, respectively.^{92,93,110} These features unambiguously lead to the conclusion that *ab initio* methods accurately reproduce bonding defects, in obvious contrast with simulations using classical force fields^{122,124} or RMC modeling.^{113–115} The origin has to be found in the treatment of the time-dependent electronic density, which gives a much better description of charge transfer in these covalent systems during the quench to the glassy state.

On the experimental side, we remark that the intensity of the main peak at $d(\text{Ge}-\text{Ge}^{\text{III}}) = 3.68$ Å in g_{GeGe} is slightly

TABLE II. Calculated real-space structural properties in amorphous $\text{Ge}_x\text{Se}_{1-x}$: first ($X-X^{\text{I}}$, $X = \text{Ge}, \text{Se}$), second ($X-X^{\text{II}}$), and third ($X-X^{\text{III}}$) peak positions (all given ± 0.02 Å), pair coordination numbers n_{ij} , coordination numbers n_i , and mean coordination number \bar{r} . The cutoff distances for the calculation of the coordination numbers have been taken at the minimum of the pair distribution functions ($r_m = 2.9$ Å). Results are compared to experimental data (Refs. 109 and 157).

	GeSe_9	GeSe_4	GeSe_3	GeSe_2
Ge-Ge^{I} (Å)			2.42	2.44 2.42 (Ref. 109)
Ge-Ge^{II} (Å)	3.05	3.01	3.01	3.03 3.02 (Ref. 109)
$\text{Ge-Ge}^{\text{III}}$ (Å)	3.63	3.65	3.59	3.68 3.57 (Ref. 109)
Ge-Se^{I} (Å)	2.35	2.36 2.36 (Ref. 157)	2.36	2.36 2.36 (Ref. 109)
Ge-Se^{II} (Å)	3.70	3.67	3.65	
Se-Se^{I} (Å)	2.38	2.36	2.36	2.37 2.32 (Ref. 109)
Se-Se^{II} (Å)	3.81	3.85	3.85	3.88 3.89 (Ref. 109)
n_{GeGe}			0.13	0.25
n_{SeGe}	0.45	1.00	1.29	1.77
n_{GeSe}	4.01	3.92	3.87	3.55
n_{SeSe}	1.56	1.00	0.71	0.30
n_{Ge}	4.01	4.01	4.01	3.80
n_{Se}	2.00	2.00	2.00	2.08
\bar{r}	2.20	2.40	2.50	2.64

higher and the decay to zero between the first and second shells of neighbors at around 4.5 Å more pronounced. In the partial g_{GeGe} , besides the homopolar distance Ge-Ge^{I} (Table II) giving rise to a so-called ethylenelike (ET) unit [Fig. 8(a)], one also finds two other main peaks at $d(\text{Ge}-\text{Ge}^{\text{II}}) = 3.03$ Å and $d(\text{Ge}-\text{Ge}^{\text{III}}) = 3.68$ Å. These can be unambiguously assigned to Ge-Ge correlations appearing respectively in edge-sharing (ES) and corner-sharing (CS) tetrahedra, as also identified by Salmon and co-workers.⁸³ The main feature of the pair distribution function g_{GeSe} consists in a very intense peak at a distance of $d(\text{Ge}-\text{Se}^{\text{I}}) = 2.36$ Å, very well separated from the secondary contributions, this first peak being identified with the Ge-Se distance defining the tetrahedra. It should be noted that a small peak is experimentally acknowledged at 3.02 Å which is not reproduced by the simulation (Fig. 7). Finally, g_{SeSe} has essentially two main contributions: the Se-Se homopolar prepeak found at $d(\text{Se}-\text{Se}^{\text{I}}) = 2.37$ Å and the main peak at $d(\text{Se}-\text{Se}^{\text{II}}) = 3.88$ Å, the latter distance being the one corresponding to Se-Se correlations defining the edge of a $\text{GeSe}_{4/2}$ tetrahedron.

All pairs g_{ij} ($i, j = \text{Se}, \text{Ge}$) can then be tracked as a function of Ge composition. The Ge-Ge pair distribution function g_{GeGe} shows large variations for the three aforementioned peaks: ET, ES, and CS. While the position and intensity of the main peak at $d(\text{Ge}-\text{Ge}^{\text{III}}) = 3.63\text{--}3.68$ Å remain nearly unchanged (Table II), we find that homopolar bonding appears only for the Ge-rich compositions GeSe_3 and GeSe_2 . These findings are consistent with those obtained from Raman experiments where typical modes associated with the homopolar Ge-Ge

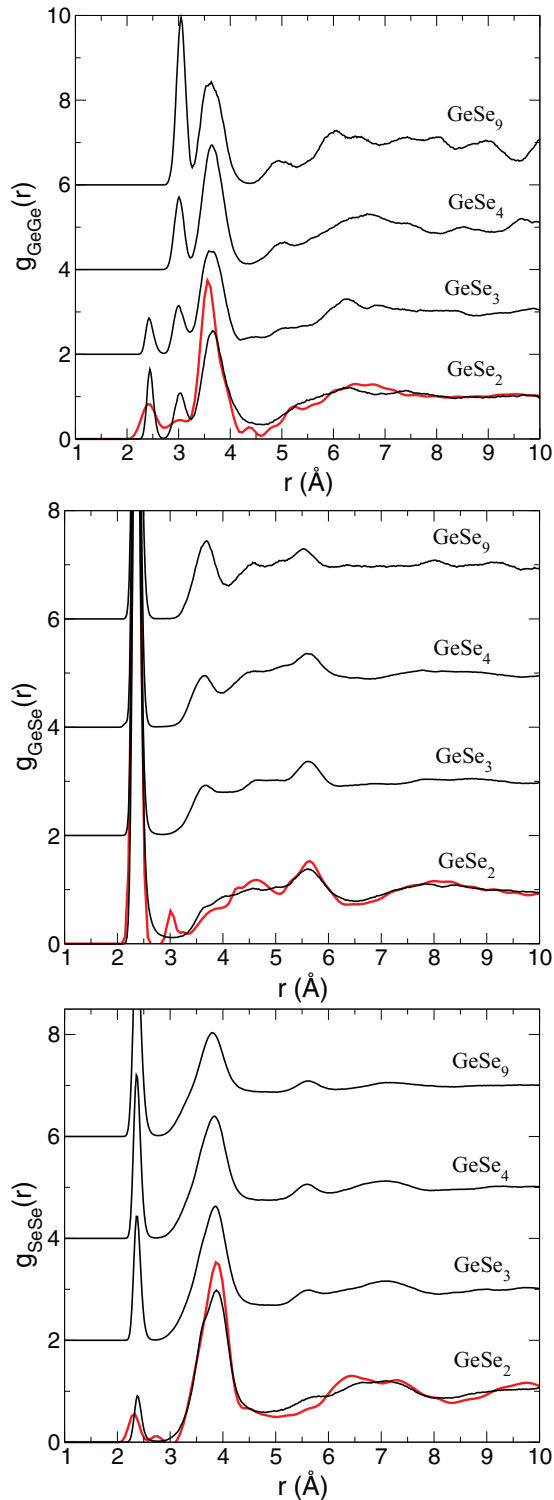


FIG. 7. (Color online) Computed pair distribution functions g_{ij} ($i, j = \text{Ge, Se}$) as a function of composition x in $\text{Ge}_x\text{Se}_{1-x}$ glasses, compared to results from isotopic substituted neutron diffraction (red curve, Refs. 83 and 110).

ET units bonds are detected only for concentrations at or somewhat below 30% Ge.¹⁵⁸ The precise statistics with Ge content can be established from the atomic-scale trajectories, as discussed below. The intensity of the ES peak at 3.03–3.05 Å is reduced in going from GeSe_9 to GeSe_2 , indicating that the

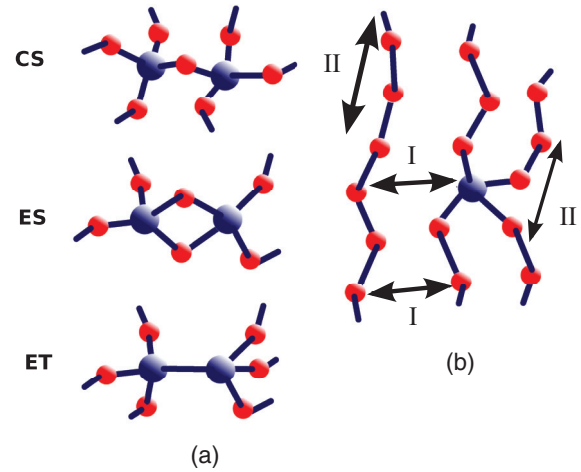


FIG. 8. (Color online) (a) Typical local connections between two Ge units: corner-sharing (CS) $\text{GeSe}_{4/2}$ tetrahedra, edge-sharing (ES) tetrahedra, and ethylenelike (ET) unit involving a homopolar Ge-Ge bond. (b) A typical representation of a Se-rich glassy network of $\text{Ge}_x\text{Se}_{1-x}$, showing possible inter- or intrachain correlations (arrows I and II) between Se and Ge and a neighboring Se atom, which involve the distances $d(\text{Ge}-\text{Se}^{\text{II}})$ and $d(\text{Se}-\text{Se}^{\text{II}})$, respectively (see also Fig. 9).

GeSe_9 composition contains a large fraction of such motifs [Fig. 8(a)], as also independently established from the ring statistics analysis and the bond angle distribution described below.

There are virtually no changes with composition in the first peak defining the Ge-Se bond distance $d(\text{Ge}-\text{Se}^{\text{I}}) = 2.35\text{--}2.36$ Å of the $\text{GeSe}_{4/2}$ tetrahedron. The most interesting information that can be gathered from the g_{GeSe} partial is the evolution of the secondary peak found at $d(\text{Ge}-\text{Se}^{\text{II}}) = 3.70$ Å in GeSe_9 . Its intensity is decreasing as the Ge content is increased. For this GeSe_9 composition, a detailed inspection of the atomic trajectories shows that this peak can be assigned (i) to the distance between a cross-linking Ge atom and a neighboring Se chain [the arrows I in Fig. 8(b) and red curve in Fig. 9], and (ii) to the second-nearest-neighbor distance along a Se chain [the arrows II in Fig. 8(b) and blue curve in Fig. 9]. The latter characteristic distance can be roughly evaluated to $2d(\text{Se}-\text{Se}^{\text{I}}) \sin \theta_{\text{Se}-\text{Se}-X}/2$ ($X = \text{Ge, Se}$) = 3.65 Å given the calculated value of the corresponding bond angle $\theta_{\text{Se}-\text{Se}-X} = 100^\circ$ (see below). In the case where a $\text{GeSe}_{4/2}$ tetrahedron is involved, the corresponding Se-Se distance is equal to $\sqrt{8/3}d(\text{Ge}-\text{Se}^{\text{I}}) = 3.85$ Å. These typical distances are very close to those contributing to g_{SeSe} at nearly the same distance [the arrows I and II in Fig. 8(b)]. They are also close to the interchain correlation distance of 3.69 Å found in amorphous selenium¹⁵⁹ where only Se polymeric chains are present. This identification simply reveals that at low Ge content, replacing a Ge into a Se chain involves the same correlation distance with a neighboring chain. However, as the Ge content and the mean coordination number \bar{r} increase, a fully cross-linked network emerges. The intensity of this secondary peak in g_{GeSe} decreases, as already detected for the GeSe_4 composition (Fig. 7). It is the signature that such interchain correlation distances contributing to $d(\text{Ge}-\text{Se}^{\text{II}})$ at low x are vanishing, the second-shell Ge-Se neighbor distances now being mostly originated by the random connection of $\text{GeSe}_{4/2}$ tetrahedra.

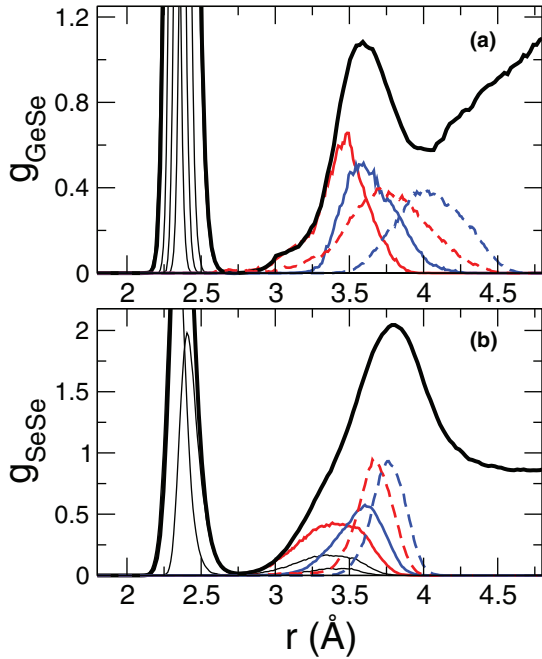


FIG. 9. (Color online) Pair distribution functions g_{GeSe} and g_{SeSe} in GeSe_9 (thick black line, as in Fig. 7) and decomposition into neighbor distributions. (a) Fifth (red) and sixth (blue) Se neighbors around a Ge atom, compared to corresponding distributions in GeSe_2 (broken curves). (b) Third (red) and fourth (blue) Se neighbors around a Se atom, compared to corresponding distributions in GeSe_2 (broken curves). Solid red curves merely correspond to arrows I in Fig. 8, and solid blue curves to arrows II.

As a result, the fifth- and sixth-neighbor distributions broaden and shift in position, while having a reduced intensity [broken curves in Fig. 9(a)]. This leads to an important reduction of the peak at $d(\text{Ge}-\text{Se}^{\text{II}})$ which is barely visible at the GeSe_2 composition. This situation contrasts with the one observed in the partial g_{SeSe} where the intensity of the secondary peak at $d(\text{Se}-\text{Se}^{\text{II}}) \simeq 3.81 \text{ \AA}$ increases, while also becoming sharper (Fig. 7). It signals that the main contribution to this peak in GeSe_9 is due to Se-Se interchain and second-chain-neighbor correlations, which are reduced as the concentration of Ge is increased. The $\text{GeSe}_{4/2}$ tetrahedra involving a Se-Se distance (the edge of the $\text{GeSe}_{4/2}$ tetrahedra) become then the dominant contributors to Se-Se correlations [broken lines in Fig. 9(b)] for $d(\text{Se}-\text{Se}^{\text{II}})$ in GeSe_2 .

B. Coordination numbers and bond angle distributions

1. Coordination from pair distribution functions

From the pair distribution functions of Fig. 7, we obtain by integrating up to the first minimum ($r_m = 2.9 \text{ \AA}$) the partial coordination numbers n_{GeGe} , n_{SeGe} , and n_{SeSe} for different compositions (Table II). Note that one has $(1-x)n_{\text{SeGe}} = xn_{\text{GeSe}}$. When one changes from GeSe_9 to GeSe_2 , a decrease of the Ge-Se partial coordination number is found, which results from the onset of homopolar Ge-Ge bonds (ET unit) and an increase of n_{GeGe} once $x \geq 25\%$ Ge, leading to $n_{\text{GeGe}} = 0.25$ at the stoichiometric composition (GeSe_2). Additional details on the neighbor statistics are provided below. From such numbers, the Ge and Se coordination numbers can be

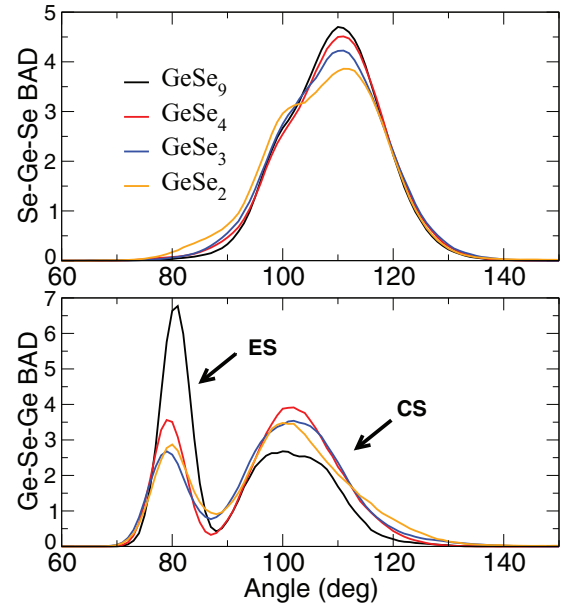


FIG. 10. (Color online) Computed Se-Ge-Se (top) and Ge-Se-Ge (bottom) bond angle distributions in $\text{Ge}_x\text{Se}_{1-x}$ glasses for different Ge compositions. These distributions have been calculated by including neighbors separated by less than 2.9 \AA .

computed from $n_{\text{Ge}} = n_{\text{GeGe}} + n_{\text{GeSe}}$ and $n_{\text{Se}} = n_{\text{SeGe}} + n_{\text{SeSe}}$, and results are given, again, in Table II. These show that for the nonstoichiometric compositions (GeSe_9 , GeSe_4 , and GeSe_3), one has coordinations that follow directly the octet rule, i.e., $n_{\text{Ge}} \simeq 4$ and $n_{\text{Se}} \simeq 2$. For the stoichiometric compound, the presence of the ET unit and the occurrence of coordination defects (see below) reduce the overall Ge coordination number ($n_{\text{Ge}} = 3.80$) while slightly increasing that of selenium ($n_{\text{Se}} = 2.08$) because of the presence of a small amount of threefold-coordinated Se.

2. Bond angle distribution

In Fig. 10 we show the Se-Ge-Se (θ_{SeGeSe}) and Ge-Se-Ge (θ_{GeSeGe}) bond angle distributions. Two main features emerge. First, the Se-Ge-Se bond angle distribution appears to be highly symmetric around 109° at low modifier content, indicative of an increased tetrahedral order when compared to the same distribution for GeSe_2 , which contains a tail at lower angles and also a lower intensity. These modifications appear to be linked to the increased presence of defect coordinations (see below) which display other preferential angles, e.g., 100° for a fivefold-coordinated germanium (Ge^{V}). This effect becomes even more pronounced when a composition with a high Ge content is considered, consistently with the increase of Ge^{V} for GeSe_2 (Table III). Second, two distinct peaks are clearly visible in the Ge-Se-Ge bond angle distribution at about 80° and 100° . These can be associated with edge-sharing and corner-sharing tetrahedra, respectively [Fig. 8(a)]. The ES peak is intense at low Ge content (GeSe_9) and decreases in amplitude when the Ge composition increases. It suggests that the fraction of ES units is larger and dominates the tetrahedral bonding in GeSe_9 , as also characterized independently from the ring statistics.

TABLE III. The proportion of the different coordination units in glassy Ge-Se systems for the five compositions of interest. The percentage of the central atom α (Ge^{*i*} or Se^{*i*}) that has i neighbors is given in bold font. The fraction of homopolar bonds among a given species (0,1,2,3) is given in the next columns. The cutoff distances for the calculation of the coordination numbers have been taken at the minimum of the pair distribution functions ($r_m = 2.9$ Å).

System	α	0	1	2	3	
GeSe ₉	Ge ^{IV}	96.5	96.5			
	Ge ^V	3.5	0.1	3.4		
	Se ^I	0.2	0.2			
	Se ^{II}	97.3	7.3	28.4	61.6	
	Se ^{III}	1.5			0.8	0.7
GeSe ₄	Ge ^{II}	1.1	1.1			
	Ge ^{III}	0.3	0.3			
	Ge ^{IV}	96.2	96.2			
	Ge ^V	4.8		4.8		
	Se ^I	0.5	0.4	0.1		
GeSe ₃	Se ^{II}	98.3	27.9	41.9	28.4	
	Se ^{III}	1.2	0.1	0.2	0.4	0.5
	Ge ^{IV}	96.5	86.9	9.6		
	Ge ^V	3.5	0.1	3.0	0.4	
	Se ^I	0.4	0.4			
GeSe ₂	Se ^{II}	97.6	42.3	41.6	13.7	
	Se ^{III}	2.0	0.6	0.6	0.8	
	Ge ^{II}	1.6	1.6			
	Ge ^{III}	11.1	11.1			
	Ge ^{IV}	81.9	60.7	21.2		
Ge ₂ Se ₃ (Ref. 51)	Ge ^V	4.4	0.3	3.9	0.2	
	Se ^I	0.1		0.1		
	Se ^{II}	91.7	71.4	18.1	2.3	
	Se ^{III}	8.2	5.6	1.9	0.6	0.1
	Ge ^{II}	3.5	3.0	0.5		
	Ge ^{III}	20.0	15.5	4.5		
	Ge ^{IV}	74.0	35.0	34.0	5.0	
	Ge ^V	1.7	0.1	0.8	0.8	
	Se ^I	0.1	0.1			
	Se ^{II}	82.0	82.0			
	Se ^{III}	14.7	14.6	0.1		
	Se ^{IV}	0.2	0.2			

3. Coordination details from neighbor analysis

From the detailed analysis of neighbors (Table III), we now focus on the way the homopolar bondings are distributed among species of a given coordination, as in Ref. 135. As represented and discussed above (Fig. 7), homopolar Ge-Ge bonds appear at the composition GeSe₃ and then grow continuously up to the Ge₂Se₃ composition.⁵¹

In fact, further insight into the network topology and its change with composition can be obtained by following the coordination distributions Ge^{*i*} and Se^{*i*} ($i = \text{I, II, III, IV, V}$) around given species. These quantities are defined as the average number of atoms of a given species (Ge, Se) that are l -fold coordinated (Table III). As a first observation, one notices that the dominant coordination is of course Ge^{IV} and Se^{II} as also determined from the integration of the pair distribution functions (Table II) or observed from the first four neighbor distributions contributing to the first peak (2.35 Å) in the g_{GeSe} pair distribution functions in, e.g., GeSe₉ (Fig. 9).

For compositions belonging to the flexible and the intermediate phases (GeSe₉, GeSe₄, and GeSe₃), the fraction of such species is found between 97% and 98%, underscoring the tendency towards a network with components fulfilling merely the $8 - N$ (octet) rule. Coordination defects such as Ge^V and Se^{III} are found to be low (<3%) whereas Ge^{III} is absent. At higher compositions (GeSe₂) however, threefold-coordinated species increase substantially (11.1%) and lead to a network that contains a larger fraction of miscoordinated atoms, this situation being also encountered for the Se atoms which show a decrease in Se^{II} coordination from 97.6% to 91.7% between GeSe₃ and GeSe₂. The increase of Ge content leads to enhanced chemical disorder with larger amounts of bonding defects.⁵¹

The detail of the bonding scheme on each of these l -fold-coordinated species shows that most of the homopolar Ge-Ge bonds are always found as single defects on Ge^{IV} species, i.e., one has predominantly one homopolar bond among the four bonds, i.e., a majority of GeGeSe₃ and no Ge₂GeSe₂ units for $x < 40\%$.

C. Ring statistics and medium-range structure

The topological intermediate-range order can be characterized using a ring statistics algorithm which has been applied for all compositions from the rigorous investigation of networks generated using simulation (RINGS) code.¹⁶⁰ A cutoff distances of 2.9 Å has been used for all atomic pairs (Ge-Ge, Ge-Se, and Se-Se), corresponding to the minimum r_m of the pair distribution functions (Fig. 7). The algorithm is mostly based on the King¹⁶¹-Franzblau¹⁶² shortest-path search to find rings containing a maximum of 14 atoms. In addition, such a statistical search can be refined by considering either every atom during the ring search mode, or a selected type (e.g., Ge).

Figure 11 displays the ring statistics $R^{(n)}$ for five compositions in the amorphous Ge-Se system, including Ge₂Se₃.⁵¹ First, one should note that all sizes n of rings are involved, i.e., both odd- and even-sized rings. For the stoichiometric composition ($x = 33\%$), this situation contrasts with corresponding oxide glasses (SiO₂, GeO₂), which have only heteropolar bonds, and lead only to even-sized rings.^{163,164} It results from the presence of homopolar Ge-Ge or Se-Se bonds (see Fig. 7) which allows the possibility of having closed loops of odd size, a direct indication that the corresponding ring will contain homopolar bonds. As these are found at all compositions (Se-Se for chalcogen rich and Ge-Ge close to the stoichiometric GeSe₂), odd rings are encountered for all investigated compositions. Inspection of Fig. 11 shows that the increase of Ge composition x tends to increase the number of possible ring structures. At low Ge content (i.e., GeSe₉), one finds only a limited number of rings ($R^{(n)} < 4$ whatever the size n) due to the chainlike nature of the network backbone which prevents formation of small ($n = 4-7$) and, moreover, intermediate-sized ($n = 8-14$) rings. A search of closed loops of sizes larger than $n = 14$ (not represented) shows that such chalcogen-rich systems have rings containing up to 18–20 atoms. For the chalcogen-rich composition GeSe₉, no evidence of possible Se₈ is found. These have been detected from the structural analysis of crystalline selenium¹⁶⁵ while

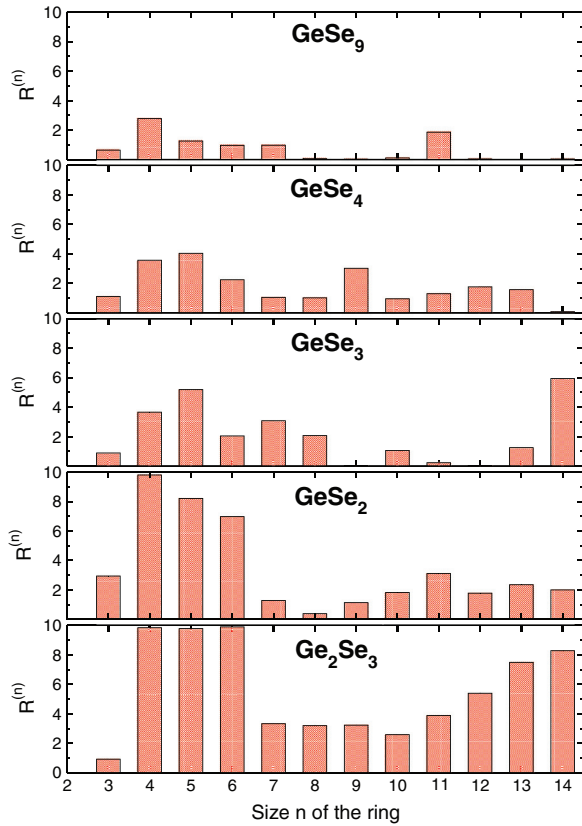


FIG. 11. (Color online) Calculated number of rings $R^{(n)}$ in amorphous $\text{Ge}_x\text{Se}_{1-x}$ for different Ge compositions using the RINGS method (Ref. 160).

ring structures have been detected in the liquid and amorphous phases.^{166,167} Here, one finds only the presence of a large-sized ring ($R^{(11)}$) (Fig. 11) which may be reminiscent of such closed loops in the base Se glass.

1. Connection with the outrigger raft model

The growth of the Ge content leads to an overall increased cross-linking tendency which manifests by a global growth of all types of rings.¹⁶⁰ However, the distribution is dominated by smaller rings having $n < 7$, i.e., rings containing either four [ES motifs, Fig. 8(a)], five, or six atoms. These are the elementary building blocks that appear in the outrigger raft model proposed by Phillips and co-workers¹⁶⁸ on the basis of the structure¹⁶⁹ of crystalline GeSe_2 , and which has been extensively discussed in the literature.^{49,170–172} For this compound, our computed ring ratio for four-, five-, and sixfold rings is 10:8:7, i.e., quite different from the one extracted from the outrigger raft structure, which is 1:2:2 (specifically Fig. 2 in Ref. 168). Moreover, within this picture,¹⁶⁸ only fivefold rings ($R^{(5)}$) contain Se-Se homopolar bondings, whereas Ge-Ge bonds are not proposed. From a detailed analysis of our ring statistics result (Table IV), one finds not only that fivefold rings can contain a variety of bonding motifs with one, two, or three Ge atoms, but also that six-membered rings (fully heteropolar in the outrigger raft model) have homopolar bonds as well. The ratio of the three bonding types (Ge-Ge, Ge-Se, Se-Se) within such rings strongly depends on the Ge content as can be seen in Table IV. For instance, in GeSe_2 fivefold

TABLE IV. Calculated distribution of Ge atoms (in %) within five- and six-membered rings, using the RINGS analysis (Ref. 160). The second column indicates the number $n(\text{Ge})$ of Ge atoms that are part of a given ring.

Ring	$n(\text{Ge})$	GeSe_9	GeSe_4	GeSe_3	GeSe_2	Ge_2Se_3
5	1	0.4			12.3	
	2	80.7	100.0	100.0	14.1	2.7
	3	18.9			73.6	96.4
	4					0.8
6	2		3.0	50.4	28.5	
	3		88.3	49.6	71.5	85.4
	4					14.6

rings contain a fraction of $n(\text{Ge}) = 12.3\%$, 14.1% , and 73.6% for one, two, and three Ge atoms, respectively. From this statistics, one realizes that the fivefold ring motif proposed in the outrigger raft model for GeSe_2 [two Ge atoms and four Se atoms,¹⁶⁸ i.e., fivefold rings with $n(\text{Ge}) = 2$], has an occurrence of only 14.1% (Table IV) but surprisingly 100% for the IP compositions GeSe_4 and GeSe_3 . This ratio then decreases to 2.7% for Ge_2Se_3 . At this composition of 40% Ge, the probability of finding small rings is equal to $R^{(n)} \simeq 10$ (Fig. 12). Larger ring structures ($n > 11$) also grow as the increase of connectivity leads to enhanced possibilities of finding large closed loops during the ring search.¹⁶⁰ Similarly, the six-membered ring which is fully heteropolar in the GeSe_2 model¹⁶⁸ contains defects which can be tracked with composition and reveal a much more complex picture than the one derived from the outrigger raft structure. For instance, the sixfold ring appears to contain a large fraction of heteropolar bonds for the GeSe_4 compound (88.3%) whereas homopolar bonds can be found at larger Ge compositions (e.g., GeSe_3).

Of special interest are the rings which contribute to the first part of the distributions shown in Fig. 11, i.e., $R^{(n)}$ with $n \leq 7$, leading usually to a distinct spectroscopic signature.^{173,174} When represented as a function of Ge composition (Fig. 12),

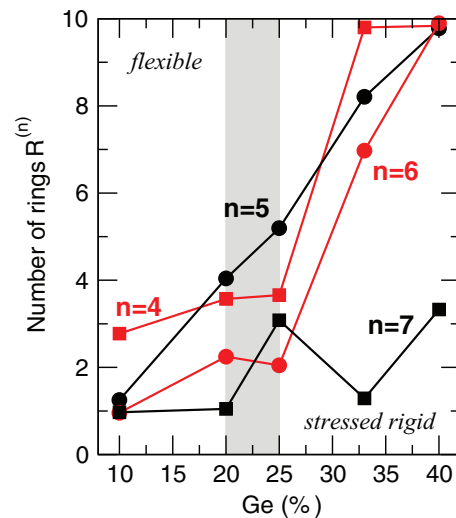


FIG. 12. (Color online) Number of small rings $R^{(n)}$ ($3 < n < 8$) in amorphous $\text{Ge}_x\text{Se}_{1-x}$ as a function of Ge composition x . The gray zone indicates the experimentally determined intermediate phase.

TABLE V. Calculated ES:CS ratio in amorphous $\text{Ge}_x\text{Se}_{1-x}$ and comparison with experimental estimates from Raman scattering (Refs. 68,96, and 175), NMR, (Ref. 175), and neutron diffraction (Refs. 110 and 157).

	GeSe_9	GeSe_4	GeSe_3	GeSe_2	Ref.
Present work	0.86	0.42	0.32	0.96	
Raman	0.20	0.18	0.21	0.35	68
	0.25	0.22	0.31	0.44	96
	0.20	0.19		0.26	175
NMR	0.31	0.25		0.37	175
Neutron				0.34	110,157

most of them display marked changes between the GeSe_3 and GeSe_2 compositions. For instance, four-, and sixfold rings show an important increase from $R^{(n)} = 2-4$ for $x \leq 25\%$ (GeSe_3) to 7–10 for the GeSe_2 composition. At low x (GeSe_9), ES motifs dominate the ring statistics, as already detected from the prominent peak at $d(\text{Ge-Ge}^{\text{II}})$ in the pair distribution function g_{GeGe} (Fig. 7) and in the ES contribution of the bond angle distribution (Fig. 10). For larger compositions, the ES structure ($R^{(2)}$) is found to remain constant while fivefold rings display a continuous increase over the whole range of composition (Fig. 12).

Can such features be related to experimental measurements? Both Raman spectroscopy^{68,96,175} and ^{77}Se NMR (Ref. 175) have followed the ES:CS ratio with composition as these two $\text{GeSe}_{4/2}$ connections lead to typical vibrational modes in, e.g., the Raman spectroscopic peaks (200 and 250 cm^{-1} , respectively⁶⁸). In the present simulation and in the absence of Ge-Ge bonds, the fraction of $\eta = N_{\text{ES}}/N_{\text{CS}}$ can be simply estimated from $\eta = 2R^{(4)}/N_{\text{Ge}}(x)$ which leads to $\eta = 0.86$ and 0.42 for GeSe_9 and GeSe_4 , respectively. To obtain the fraction of CS tetrahedra in the presence of Ge-Ge bonds, we follow the procedure used in Ref. 109 where $N_{\text{CS}} = 1 - N_{\text{ES}} - N_{\text{GeGe}}$ and N_{GeGe} is determined from the neighbor analysis (Table III). As noted earlier from independent simulations of some specific compositions,¹⁴² we do find an ES:CS ratio which is much larger than the experimental counterpart,¹¹⁰ this being especially true at large Ge content (Table V). However, it should be noted that even the experimental estimate exhibits some spread that has been attributed to sample homogeneity.⁶⁸

While the effect of the system size appears to be negligible,¹⁵⁶ the increased fraction of ES tetrahedra from FPMD simulations may actually arise from the thermal history of the amorphous systems which involves quenching rates that are much higher (10 K/ps) than the experimental counterparts.⁵⁰ A recent *ab initio* MD study on a similar system (GeS_2) has shown that indeed the medium-range order¹⁷⁶ (FSDP) and the ring statistics¹⁷⁷ are affected by the quenching rate. For this particular system, the fraction of ES tetrahedra appears to decrease with decreasing cooling rate, thus indicating an overall tendency that is consistent with the overestimation of the ES rate (Table V) of the simulated Ge-Se glasses. However, given that all amorphous compositions have been obtained with the same thermal history, the relative trends in composition of the ES rate and, more generally, the rings statistics can be considered as robust. In fact, we do find a

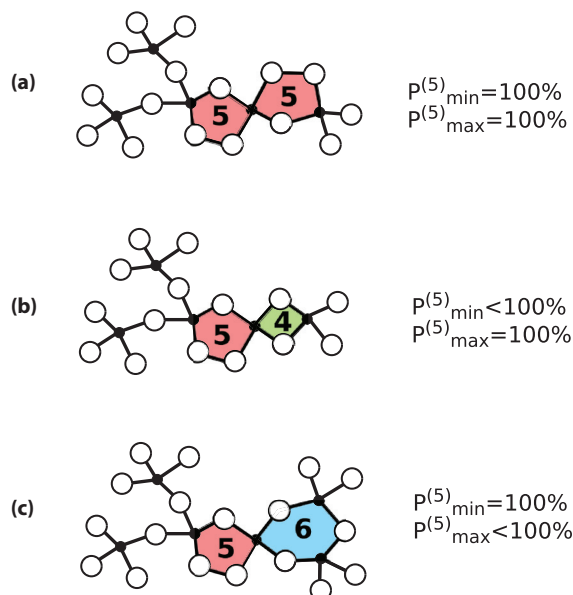


FIG. 13. (Color online) Examples illustrating the definition of (i) the probability $P_{\text{max}}^{(n)}$ that a ring of size n (here $n = 5$) is the longest closed-path solution of the analysis over Ge atoms, and (ii) the probability $P_{\text{min}}^{(n)}$ that a ring of size n (again $n = 5$) is the shortest closed-path solution of the analysis. One has $P_{\text{max}}^{(5)} = 100\%$ and $P_{\text{min}}^{(5)} = 100\%$ if any of the atoms of a considered ring (in red) connect to another ring of the same size (a). One has $P_{\text{min}}^{(5)} < 100\%$ if the considered ($n = 5$) ring contains Ge atoms which connect to a ring of smaller size [$n = 4$, green (b)]. One has $P_{\text{max}}^{(5)} < 100\%$ if the considered ($n = 5$) ring contains Ge atoms which connect to a ring of larger size [$n = 6$, blue (c)].

minimum in the ES rate for the GeSe_4 - GeSe_3 compositions, in agreement with the experimental estimates.^{68,96,175}

2. Ring correlations

The next question one can consider is the ring connectivity, i.e., one wonders if there are any correlations between rings of a given type. We define the quantity $P_{\text{max}}^{(n)}$, which is the probability that a ring of size n is the longest closed path (i.e., the largest size) having the same atom as the starting point of a search. Similarly, for a given atom in an n -fold ring, $P_{\text{min}}^{(n)}$ gives the probability that this ring is the shortest closed path having this same atom as the starting point of a search. Figure 13 illustrates these two definitions with several examples. Results for the various compositions are displayed in Fig. 14 where the probabilities $P_{\text{min}}^{(n)}$ for Ge atoms are followed with x . $P_{\text{max}}^{(n)}$ increases with n , whatever the composition (not shown). This simply indicates that when one considers a Ge atom belonging to a ring of small size n , one can always find this atom as being also part of a ring of size $m > n$ so that $P_{\text{max}}^{(n)} \simeq 0$ for most of the small n 's. For larger sizes ($n > 7$), however, it becomes more difficult to find such Ge atoms in rings of size $m > n$ so that $P_{\text{max}}^{(n)}$ becomes nonzero. Of special interest is the composition $x = 10\%$, for which $P_{\text{max}}^{(n)}$ peaks at $n = 5$ with a probability close to 90% (not shown). These findings (Fig. 13) indicate that the fivefold rings are either isolated or always connected to fivefold or fourfold rings (in the latter case $P_{\text{min}}^{(n)} = 100\%$; see below).

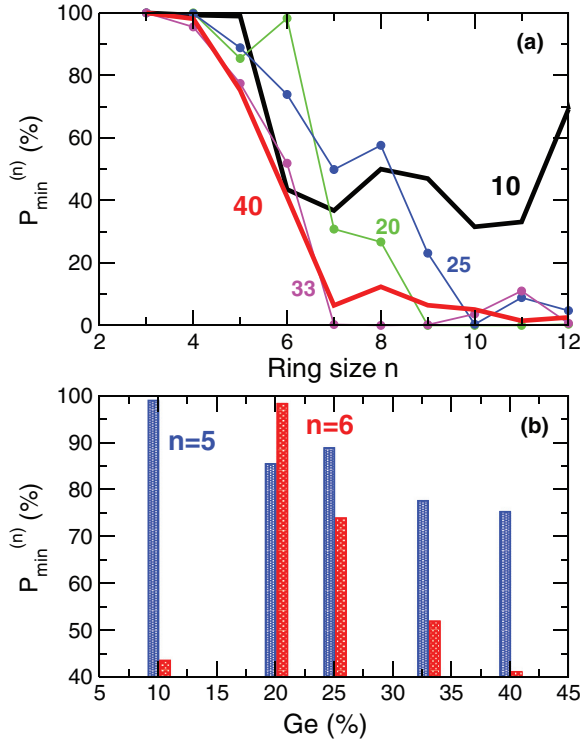


FIG. 14. (Color online) Ring connectivity (Ref. 160): (a) $P_{\min}^{(n)}$ for different Ge compositions in amorphous $\text{Ge}_x\text{Se}_{1-x}$ with x ranging from 10% (GeSe_9) to 40% (Ge_2Se_3). Results of the two end compositions [10% (GeSe_9) and 40% (Ge_2Se_3)] are represented in thick lines. (b) Evolution of $P_{\min}^{(n)}$ with composition, for five- ($n = 5$) and sixfold ($n = 6$) rings.

The quantity $P_{\min}^{(n)}$ behaves in exactly the opposite way, i.e., $P_{\min}^{(n)} = 100\%$ for small n , because it is difficult for a given size n to find a Ge atom belonging also to a ring of size $p < n$. As the Ge composition and thus the number of small rings ($n < 7$) increases (Fig. 12), one expects indeed to see $P_{\min}^{(n)}$ decrease for any size n because the increase in network connectivity will lead to the occurrence of smaller loops during the ring search. However, important changes take place with composition, and these are represented in Fig. 14(a). First, one remarks that at high Ge compositions (33% and 40%) nearly all rings with $n > 7$ connect to smaller ones as $P_{\min}^{(n)} \simeq 0$. This is not the case for lower compositions since $P_{\min}^{(n)} \neq 0$ when $n < 10$ for, e.g., GeSe_3 . The smaller-ring connectivity ($n = 5, 6$) can be followed with composition [Fig. 14(b)] and one finds a continuous decrease of $P_{\min}^{(5)}$, which is consistent with the overall increase of the network connectivity. On the other hand, a nonmonotonic variation for the sixfold-ring connectivity is found. In fact, the probability $P_{\min}^{(6)}$ is maximized for the particular composition GeSe_4 . At low Ge composition, one does not expect to find an important number of Ge atoms so that correlations between two rings of the same type (i.e., leading to $P_{\min}^{(6)} = 100\%$) are rare, i.e., $P_{\min}^{(6)} \simeq 45\%$ for GeSe_9 . More surprising is the important growth to nearly 100% for the GeSe_4 composition [Fig. 14(b)] which underscores a clear tendency to cluster sixfold rings whenever possible.

The resulting picture can be established as follows in the context of flexible-to-rigid transitions: In the flexible phase (GeSe_9) one has only has small rings (four, five, and six

membered) and these tend to be isolated [Figs. 11 and 14(b)]. In the IP, the number of rings does not increase substantially with composition (Fig. 12) but the way these rings connect together changes, promoting some specific ring correlations ($P_{\min}^{(6)} = 100\%$). In the stressed rigid phase, the number of rings increases abruptly for $n = 4$ and 6 whereas $P_{\max}^{(n)}$ and $P_{\min}^{(n)}$ tend to decrease as more and more ring correlations between various sizes are now possible.

V. CONNECTION WITH BOND MODELS AND WITH TOPOLOGICAL CONSTRAINTS

A. Statistical bond models

Having established the distribution of various bonds and coordination numbers with composition (Table III), one can now check the validity of simple models for chemical ordering in Ge-Se. These cannot be discussed on the basis of pair distribution functions alone [e.g., the Bhatia-Thornton $g_{\text{NN}}(r)$ as emphasized in Ref. 83]. In fact, such simple models are usually based on a network which is supposed to follow the $(8 - N)$ octet rule, leading to 100% $n_{\text{Ge}} = 4$ and $n_{\text{Se}} = 2$, a situation that is not fully realized as shown from our detailed neighbor distribution analysis (see Table III).

1. Simple pair models

According to the random covalent network (RCN) model,^{178,179} one has a purely statistical distribution of bonds of probability $p_{ij}^{\text{RCN}} \propto W_{ij}x_i x_j$ where x_i and x_j ($i, j = \text{Ge, Se}$) are the concentrations of the species Ge and Se, and $W_{ij} = (2 - \delta_{ij})n_i n_j$ is a statistical factor taking into account the number of equivalent ways to connect two species together and involves the coordination numbers n_{Ge} and n_{Se} , δ_{ij} being the Kronecker symbol. With the normalization condition $\sum_{i,j} p_{ij}^{\text{RCN}} = 1$, one has, e.g.,

$$p_{\text{GeGe}}^{\text{RCN}} = \frac{16x^2}{\bar{r}^2}, \quad (4)$$

$$p_{\text{GeSe}}^{\text{RCN}} = \frac{8x(1-x)}{\bar{r}^2}. \quad (5)$$

An alternative model, the chemically ordered (CON) model,^{178,180,181} suggests that only Ge-Se and Se-Se bonds are possible in the Se-rich ($x < 33\%$) region, whereas Ge-Ge and Ge-Se bonds populate the network only for compositions larger than 33% (GeSe_2), given that one will now have an excess of germanium regarding stoichiometric balance. This definition leads to, e.g., $p_{\text{SeSe}}^{\text{CON}} \propto (1 - 3x)$ and $p_{\text{GeSe}}^{\text{CON}} \propto x$ for $x \leq 1/3$. At the stoichiometric GeSe_2 , a fully heteropolar Ge-Se bonded network is proposed, which is already contradicted by both simulation and experimental findings (Fig. 7). The validity of such models have been discussed recently on the basis of NMR experiments.^{175,182} Correlations at the next level (triplets) have been proposed in a similar fashion, assuming that the probability of having Se-Se-Se will vanish at some typical composition, e.g., at the mean-field rigidity transition $x = 0.20$,¹⁸³ or at the stoichiometric GeSe_2 .¹⁰⁵ Similarly, a self-organized size-increasing cluster (SIC) model has been proposed to account for the rigid intermediate phase^{24,73,184} and leads also to the statistics of such triplets. Here, Se chains and $\text{GeSe}_{4/2}$ tetrahedra connect together but stressed rigid CS

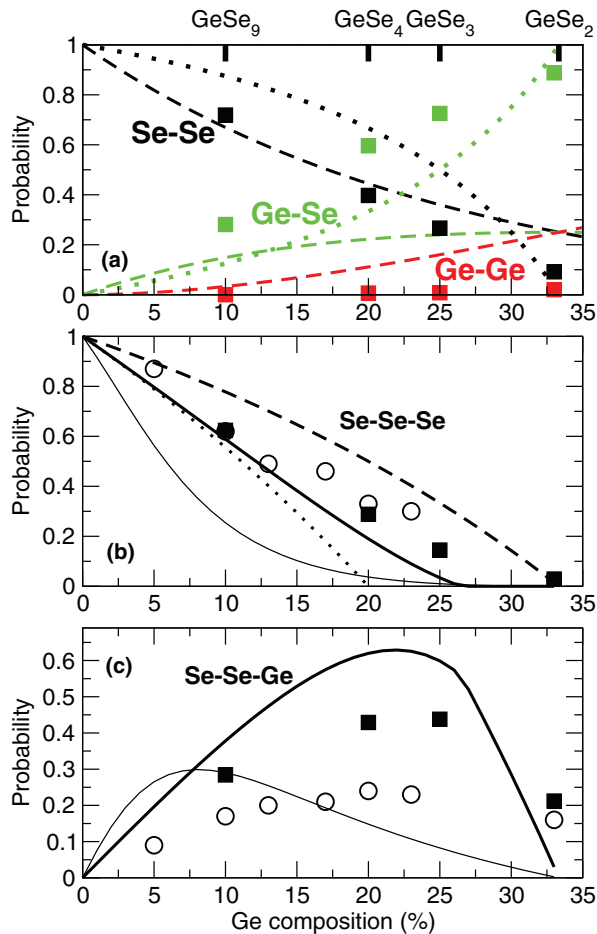


FIG. 15. (Color online) Comparison of the computed bonding statistics of the FPMD simulations with simple bond models: (a) Pair models: Random covalent network model (Refs. 178 and 179) (RCN, broken lines) and chemically ordered model (Refs. 178, 180, and 181) (CON, dotted lines) of Se-Se (black), Ge-Se (green), and Ge-Ge (red) bonds compared to FPMD results (filled squares). (b) Triplet models for Se-Se-Se: Fully clustered model (Ref. 183) (dotted lines), chain-crossing model (Ref. 105) (broken line), and size-increasing cluster model in the random (Ref. 185) (thin solid line) or self-organized (Ref. 24) (thick solid line) case, compared to results from NMR [open circles (Ref. 175)] and the present simulations (filled squares). (c) Triplet models for Se-Se-Ge: Similar comparison.

tetrahedral connections are avoided to favor ES structures. In summarizing all these simple models of amorphous Ge-Se networks, it should be emphasized that (i) all models follow the $8 - N$ (octet) rule which leads to fourfold-coordinated germanium and twofold-coordinated selenium and neglect the possibility of having coordination defects, and (ii) all models except the RCN model neglect the possibility of having Ge-Ge homopolar bondings.

From the bond statistics calculated (Table III), one can discuss the validity of these models. First, one realizes that the simple bond statistics (Se-Se, Ge-Se, Se-Se) is neither random (RCN) nor chemically ordered (CON) as shown in Fig. 15(a). In fact, we notice that the statistics of, e.g., Ge-Se is by far much larger than the one predicted by these simple models.^{178,180} As the determined fraction of Ge-Ge is rather small (but nonzero) in the simulations, the disagreement is certainly worse for the

random covalent network case, which assumes a continuous increase of Ge-Ge bonds up to a probability of 25% for GeSe₂.

2. Triplet models

Similarly, we compare our results with the triplet statistics Se-Se-Se [Fig. 15(b)] and Se-Se-Ge [Fig. 15(c)] derived from other sets of models^{24,105,183} and with experimental results from NMR.^{175,182} It is found that the statistics of Se-Se-Se bonds determined from our FPMD simulations agrees quite remarkably with that determined from NMR [Fig. 15(b) and Ref. 175], at variance with the other reported statistics (Se-Se-Ge) for which a factor of 2 difference between calculated and measured values is found. However, the same trend with composition is obtained, i.e., a bond statistics which is maximized for the IP compositions GeSe₄ and GeSe₃ [Fig. 15(c)]. When our results are compared to simple triplet models, it is found that bonding correlations do not follow a random network description (thin solid line and Ref. 185) taking into account all possible connections between Se chains and GeSe₂ tetrahedra, including the ES connection between two GeSe_{4/2} tetrahedra. When comparing such triplet statistics [Figs. 15(b) and 15(c)] with the results from the present simulation, the closest agreement is obtained for the self-organized cluster model²⁴ but it should be recalled that it does not assume Ge-Ge bonds, and thus fails to describe the entire compositional range of interest.

B. Link with topological constraints

In order to link the atomic-scale trajectories with the simple topological constraint count, we now analyze the rigidity of the different compositions by applying recently introduced methods for computing bond-stretching (BS) and bond-bending (BB) topological constraints.^{187,188} We recall that in the mean-field count^{21,22} one has five BB and two BS constraints for the Ge atom, and one BB and one BS constraint for the Se atom, so that the total number of constraints²⁴ is $n_c = 2 + 5x$. However, this count does not provide any connection with the simulated atomic structure, assumes the octet rule, and neglects chemical disorder. Neither does it take into account self-organization, accounting for the emergence of an IP on the basis of phenomenological models.^{24,74}

The number of BS constraints can be directly estimated from the evaluated coordination numbers n_{Ge} and n_{Se} (Table II), showing that these will lead to the anticipated value obtained from the simple Maxwell count, i.e., $n_c^{BB} = xn_{Ge}/2 + (1-x)n_{Se}/2$, as also indicated by the calculated value of the mean coordination number \bar{r} (Table II) and from the low radial excursion between pairs of atoms.¹⁸⁷ It appears that most of the effect of stressed rigidity can be detected from the angular motion but instead of treating angles on average at a global level,¹⁴³ a different analysis can be made which leads to additional insight.

During the simulation, the angular motion of each individual atom k is followed and this leads to a bond angle distribution $P_k(\theta)$, which can be characterized by a first moment $\bar{\theta}_k$ and a second moment (or standard deviation σ_{θ_k}). The former provides a measure of the mean angle, the latter representing a measure of the strength of the underlying angular or three-body interaction. If σ_{θ_k} is small (typically

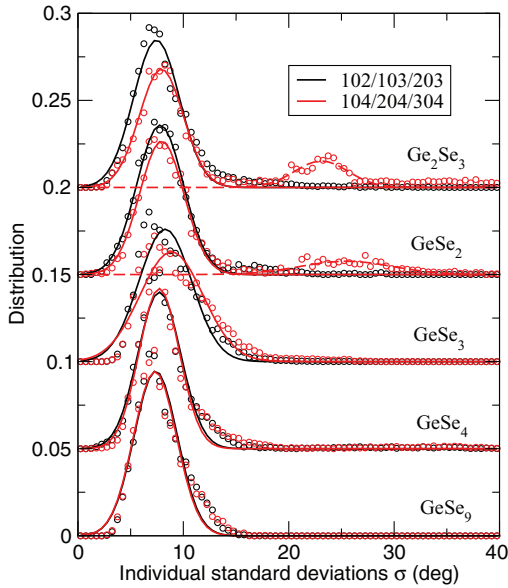


FIG. 16. (Color online) Distribution of Ge angular standard deviations for different compositions in the Ge-Se system. The total distributions have been split depending on the neighbor number: angles involving the first three neighbors (102, 103, 203, black symbols), and the fourth neighbor (104, 204, 304, red symbols). Here 0 represents the central atom and the numbers 1, 2, 3, 4 the neighbors so that e.g. the angle 102 involves the two first neighbors of the central Ge (0) atom. The solid curves are Gaussian fits which serve to estimate the population of broken constraints at high x content.

5° – 10°), it indicates that the corresponding BB restoring force which maintains the angle fixed around its mean value θ_k can be considered as an active BB constraint and will contribute to network rigidity. One can of course use the opposite reasoning when large values of σ_{θ_k} are found, and these result from large angular motions which are associated with ineffective constraints. Once the analysis is performed over the whole system (i.e., k), one obtains a distribution $f(\sigma)$ of standard deviations which can be analyzed and tracked as a function of composition or temperature¹⁸⁷ or even pressure.¹⁸⁹

Figure 16 shows the distribution of Ge-centered angular standard deviations $f(\sigma)$ for the five compositions in the Ge-Se system. The analysis has been also performed on the additional⁵¹ composition (Ge_2Se_3). For the flexible GeSe_9 and intermediate GeSe_4 compositions, one finds a single distribution for all six involved angles (102, ..., 304) located at low $\sigma \simeq 8^\circ$ – 9° indicative of a weak angular intratetrahedral motion. However, for larger compositions corresponding angles involving the fourth neighbor (104, 204, 304) partly soften. As a result a bimodal distribution (red curve) is found, indicative that some angular constraints ($\sigma \simeq 22^\circ$) are now broken. An enumeration shows that the fraction ξ of broken constraints is 17.2% and 21.4% for GeSe_2 and Ge_2Se_3 , respectively. This implies a reduction of the number of Ge BB constraints by a quantity $\Delta n_c = 3x\xi$, i.e., 0.17 and 0.26 for the aforementioned compositions, so that n_c is reduced from 3.67 to 3.50 and from 4.00 to 3.74 for GeSe_2 and Ge_2Se_3 , respectively.

What is the origin of such a softening? In the stressed rigid phase, because of the high network connectivity, asymmetric

bending motions inside $\text{GeSe}_{4/2}$ tetrahedra appear as the additional cross-links force softer interactions (i.e., angles) to adapt and to break the corresponding constraint. This leads to increased angular excursions around the mean value for atomic Se-Ge-Se triplets involving the farthest (fourth) neighbor of a central Ge atom. The present argument is consistent with the well-known relationship between stressed rigidity and bond mismatch in simple bond networks:¹⁹⁰ in a disordered system, atoms with a given coordination number cannot fulfill all their bonds at the same length because of a too high bond density or network connectivity. The same happens for angles in more complex networks such as those under consideration.

VI. ELECTRONIC PROPERTIES

Figure 17 shows the electronic density of states (EDOS) for the different Ge-Se compositions. For each composition, these calculations have been extracted from a set of 50 uncorrelated configurations on which an eigenvalue (Kohn-Sham energies) computation has been performed. First, one should note that the calculated profile of the valence bands is very close to the one determined experimentally at various Ge compositions from x-ray photoemission spectroscopy^{191–193} (XPS), and are consistent with earlier theoretical work coming either from band theory^{192,194–196} or MD simulations.¹²⁶ One finds indeed an EDOS profile which contains the two (Ge,Se) 4s bands between $\simeq -15$ and $\simeq -6$ eV, well separated from the valence 4p band structure, the contribution to the latter being mostly affected by the increase of the Ge concentration. Concerning

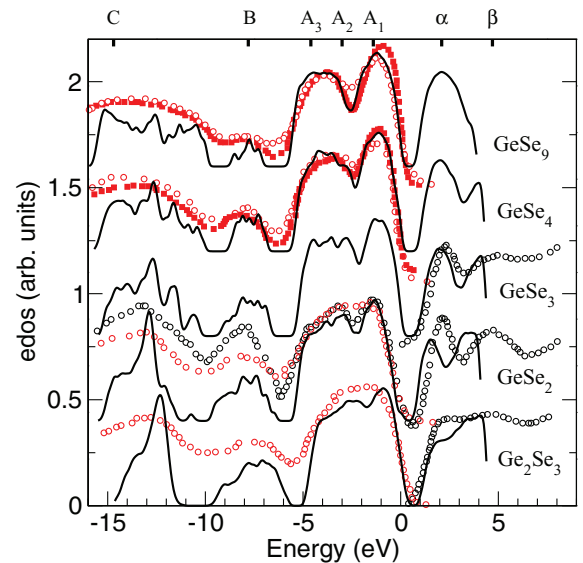


FIG. 17. (Color online) Computed electronic density of states in $\text{Ge}_x\text{Se}_{1-x}$ for different compositions (black lines). The results are compared to experimental measurements from (i) photoemission spectroscopy [black circles (Ref. 191), open red circles (Ref. 192), filled red squares (Ref. 193)] for the valence bands and (ii) inverse photoemission measurements [black circles (Ref. 198)] for the conduction band. For a better comparison along the x axis, the experimental curves have been adapted to match the valence band edge around the Fermi energy and up to the top of the A_1 peak. The upper horizontal axis shows the peak assignment established in Refs. 198 and 197 (see also Table VI).

TABLE VI. Calculated (bold character) peak energies (in eV) in the EDOS, compared to other theoretical modeling (Ref. 126) and to values obtained from photoemission (Refs. 191–193, and 197) and inverse photoemission (Ref. 198). All energies are referred to the Fermi level. Some experimental numbers have been extracted from digitalized figures. The origins of the different bands (Ge *s*, Ge *p*, etc.), determined from the calculated partial EDOSs are indicated at the bottom of the table.

System	A_1	A_2	A_3	B	C	α	β	Ref.
GeSe ₉	– 1.3		– 4.4	– 7.7	– 12.6	2.1		
	– 1.8		– 4.5	– 8.5	– 14.0			Ref. 192
	– 1.8		– 4.7	– 8.9	– 15.0			Ref. 193
GeSe ₄	– 1.1		– 4.1	– 7.7	– 12.6	2.0	4.0	
	– 1.7		– 4.0	– 8.2	– 14.0			Ref. 192
	– 1.7		– 4.1	– 8.7	– 14.0			Ref. 193
GeSe ₃	– 1.1	– 2.7	– 4.5	– 8.1	– 12.7	2.0	4.1	
						2.3	4.9	Ref. 198
GeSe ₂	– 1.3	– 2.9		– 7.4	– 12.9	1.5	3.6	
	– 1.4	– 2.7	– 4.6	– 7.0				Ref. 126
	– 1.4	– 3.0	– 4.6	– 7.8				Ref. 197
	– 2.5	– 4.7	– 6.6	– 9.5	– 14.7			Ref. 191
						2.1	4.7	Ref. 198
Ge ₂ Se ₃	– 0.8	– 2.4		– 7.4	– 12.3		4.1	
		– 2.2		– 8.2	– 13.5			Ref. 192
						2.4		Ref. 198
Origin	Se <i>p</i>	Se <i>p</i>	Ge <i>p</i> Se <i>p</i>	Ge <i>s</i>	Se <i>s</i> Ge <i>s</i>	Se <i>s</i> Se <i>p</i>	Ge <i>p</i>	

the comparison of our calculation with the previous electronic modeling of Cobb *et al.*¹²⁶ (see also Table VI), we do find an exact correspondance for the GeSe₂ compound, i.e., an intense *s* band peak at –12.9 eV (*C* peak) with a shoulder peak on the lower-energy side (Fig. 17), a somewhat broader peak (*B* peak) at –7.4 eV, and a structured *p* band consisting of an A_2 peak at –2.9 eV and an A_1 peak at –1.3 eV. At this concentration (GeSe₂), one can hardly discriminate between the A_2 peak and its companion peak A_3 , the latter having been reported at –4.6 eV from numerical¹²⁶ and experimental¹⁹⁷ studies. However, it can be seen that its energy estimation is not fully established (Table VI), and one should also have in mind that this A_3 contribution seems to be essentially a shoulder peak of the valence band peak, as discussed in Ref. 126. The relevant peaks found in the conduction band (α and β peaks; see Fig. 17) from inverse photoemission¹⁹⁸ are also reproduced with confidence from our simulations for GeSe₂, although slightly shifted when compared to Ref. 126 and to experimental data.¹⁹⁸ Table VI provides the relevant calculated and reported peak positions.

What are the effects of a change in composition? For the GeSe₉ and GeSe₄ compounds, one must first note that the valence band structure is in excellent agreement with the most recent XPS measurement from Golovchak *et al.*;¹⁹³ in particular the splitting of the valence band is clearly reproduced, with a minimum at –2.5 eV, separating the Se 4*p* (A_2 – A_3) and Ge 4*p* electronic contributions (A_1). An increase of the concentration tends to reduce such a structured band and leads for the Ge-rich Ge₂Se₃ composition to a nearly single broad band between –5 eV and the Fermi energy. We find an important change in the conduction band between the GeSe₉ and the GeSe₄ systems (Fig. 17). In fact, for the flexible composition the conduction EDOS consists of a single band centered at 2.1 eV, whereas a double contribution

is found at larger compositions and is obtained up to the stoichiometric GeSe₂. For larger compositions, the α peak found at $\simeq 2.0$ eV for smaller Ge compositions ($x < 40\%$) becomes only a shoulder of the main β peak obtained at 4.1 eV. The change obtained between GeSe₉ and GeSe₄ is in line with results from photoemission and inverse photoemission measurements, indicating an abrupt change of the valence and conduction bands at the stiffness transition,¹⁹⁹ the single broad conduction band centered around the α peak obtained in the simulation being experimentally detected up to 18% Ge. Effects of composition and the nature of the elastic phase (flexible, rigid) on electronic properties have been independently reported,²⁰⁰ and it has been shown that a maximum photosensitivity is obtained for 22% Ge, i.e., close to the centroid of the intermediate phase.

Calculation of the projection of Kohn-Sham wave functions onto the wave function associated with the atomic species allows determination of the partial contributions of Ge and Se to the EDOS. We find that Ge 4*p* electrons contribute to the first peak (α) of the conduction band, located at $\simeq 1.5$ eV for GeSe₂ [experimentally 2.1 eV (Ref. 198)], whereas Se 4*s* and 4*p* electrons contribute to both peaks (α and β) of the conduction band. This thus provides a more detailed insight into the structure of the conduction band, which has been formerly described as mainly dominated by Se *p* orbitals^{198,199} near the bottom of the conduction band.

When compared with experimental measurements,²⁰¹ the estimated optical band gap E_g (taken at the half amplitude of the A_1 peak) shows a rather good agreement (Table VII) within the typical error bars since DFT is known for gap-underestimation problems.¹⁴⁷ For the stoichiometric GeSe₂, the obtained value (1.61 eV) is somewhat lower than the one obtained from other simulations¹²⁶ (1.72 eV) but is in excellent agreement with some experimental findings (1.61 eV) for glasses investigated

TABLE VII. Calculated optical band gap energy E_g (eV) for different Ge-Se compositions, and comparison with experimental data.

	GeSe ₉	GeSe ₄	GeSe ₃	GeSe ₂	Ge ₂ Se ₃	Ref.
E_g (eV)	1.38	1.57	1.55	1.61	1.74	
	1.52	1.57		1.61	1.17	201
			1.78		1.59	202
				2.40		198

as a function of composition,²⁰¹ whereas being either under- or overestimated for other studies^{198,202,203} (2.2–2.4 eV). Note that optical gaps increase when thin films are considered^{203,204} or annealed.²⁰¹ When compared with the systematic study of Ref. 201, the global behavior of $E_g(x)$ is in excellent agreement up to the stoichiometric compound GeSe₂, i.e., one finds an increase with Ge composition from a lower value of E_g (1.38 eV for GeSe₉) to 1.61 eV for GeSe₂. Experimentally, a maximum in E_g has been reported,²⁰¹ which is not obtained here.

VII. VIBRATIONAL PROPERTIES

A. VDOS and floppy modes

The vibrational density of states $g(\omega)$ is represented in Fig. 18 for different compositions, and compared to experiments,²⁷ using the Fourier transform of the velocity-

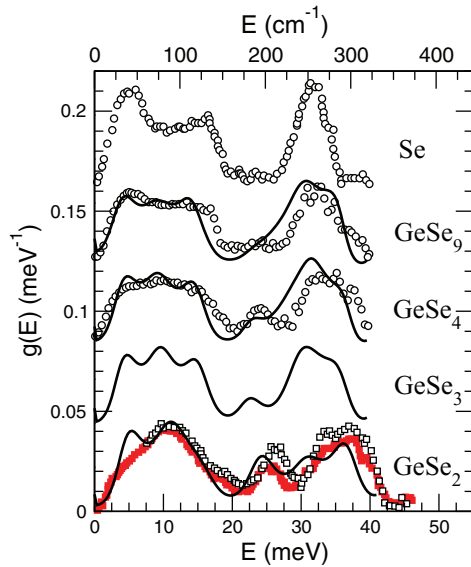


FIG. 18. (Color online) Calculated vibrational density of states (VDOS) in $\text{Ge}_x\text{Se}_{1-x}$ for selected compositions, compared to results from inelastic neutron scattering [open circles (Ref. 27), open squares (Ref. 100), red squares (Ref. 127)]. Note that the calculated VDOS of GeSe₉ is compared to experimental data (Ref. 27) on Ge₈Se₉₂. The experimental VDOS of amorphous Se is given for comparison and permits identification of the floppy mode (5 meV), and the BB (16 meV) and the BS (31 meV) energy (see Ref. 27 for details). The energy scale in cm^{-1} is provided (top axis) for a direct comparison with Fig. 21 and for the discussion (see text for details).

velocity autocorrelation function:

$$g(\omega) = \frac{1}{Nk_B T} \sum_{j=1}^N \int_{-\infty}^{\infty} \langle \mathbf{v}_j(t) \mathbf{v}_j(0) \rangle e^{i\omega t} dt. \quad (6)$$

The main features of the VDOS are very well reproduced and consist for the GeSe₂ compound of a broad band centered at 10 meV, a second band at 30–40 meV, and an intermediate contribution at 25 meV. We note a systematic redshift of the higher-frequency band (30–40 meV) of the calculated VDOS when compared to the experimental counterpart, as in previous *ab initio* modeling.^{126,127} The structure of the band is fairly well reproduced with two typical frequencies computed at 31.2 and 36.5 meV (experimentally, 33 and 36.5 meV, respectively¹⁰⁰). This discrepancy may result from the exchange-correlation functional as has already been shown for the specific case of the infrared spectrum.²⁰⁵ Gradient corrections have the general tendency to overcorrect bond lengths²⁰⁶ with the clear effect that all vibrational modes and, specifically, the stretching ones at higher frequencies, become slightly “slower” thus giving rise to the observed redshift. One should also note the spread in experimental data^{27,100} for the GeSe₂ composition. The evolution with composition is characterized by a stiffening (increase) of the higher frequencies as the system becomes rigid, whereas the low-frequency band changes only moderately at a global level and remains in excellent agreement with experimental data.

The structure of the band between 20 and 40 meV changes in an important fashion with composition as seen from the total VDOS and from the partial contributions (Figure 19). This band reduces to a single peak at 30 meV in the corresponding experimental VDOS of pure Se (Fig. 18) and is identified with Se BS vibrations.²⁷ Among different contributions, the peak at 25 meV for GeSe₂ (the so-called A₁ peak²⁰⁷) is usually

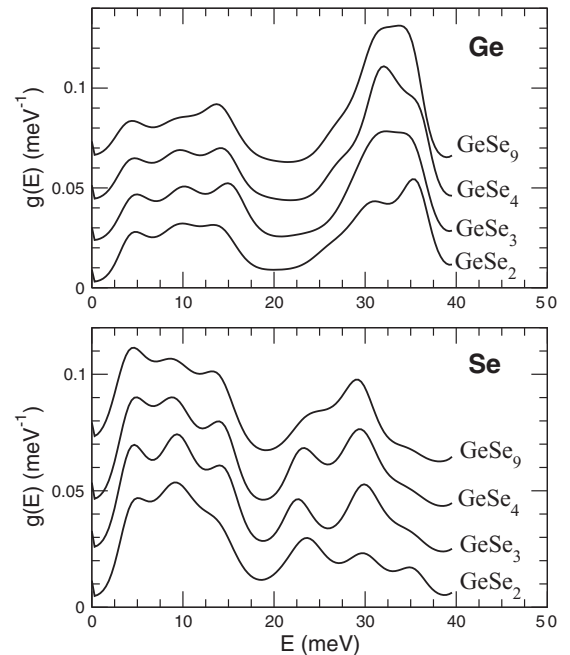


FIG. 19. Calculated partial (Ge, top and Se, bottom) vibrational densities of states (VDOS) in $\text{Ge}_x\text{Se}_{1-x}$ for selected compositions.

associated with tetrahedral A_1 breathinglike vibrations^{27,208} as also extensively discussed in the literature from results of Raman spectroscopy.^{96,168,210} Cobb *et al.*¹²⁶ determined that the motion involved in this A_1 mode contains several contributions arising not only from the breathinglike motion (in the range 24–26 meV, the A_1 peak) but also from the atomic motion of Se atoms linking edge-sharing tetrahedra (26–29 meV, the A_{1c} peak²⁰⁸). Based on our partial VDOS (Fig. 19), one realizes that these contributions have different trends with Ge composition. The higher-frequency motion associated with the A_{1c} peak is in fact much more intense for the Se-rich compositions GeSe_9 and GeSe_4 , and then decreases in intensity as the Ge content is increased. This is consistent with the dominant presence of ES motifs at those compositions (Figs. 10 and 12). On the other hand, the detail of the partials (Fig. 19) shows that the A_1 peak at $\simeq 25$ meV arises also from Se atoms but behaves in the opposite way, i.e., its intensity increases as the Se content decreases, while the peak position obviously depends on composition. These features underscore the reduction of such breathinglike motions once the network becomes more and more connected.

Finally, the low-frequency band ($E < 20$ meV) is very well reproduced from our simulations, and this holds for all compositions, especially for $E < 10$ meV. The dominant contributions to such frequencies clearly arise from Se atoms as shown in Fig. 19. For the flexible composition GeSe_9 , the VDOS does not contain any vibrational modes with zero frequency (floppy modes) as first suggested by Thorpe²¹ and Cai and Thorpe²¹⁰ from idealized bond-depleted amorphous networks constrained by a harmonic potential reproducing BS and BB forces. However, our findings are in line with the experimental results,²⁷ i.e., one does not find $g(\omega) \neq 0$ at $\omega \simeq 0$ for GeSe_9 , which would indicate the presence of zero-energy modes. One reason for the lack of such modes comes from the fact that residual forces are not taken into account in the rigidity approach²¹ (dihedral, Van der Waals, etc.) and these lead to a finite value for the floppy-mode energy, of about 5 meV, clearly observed in the experimental VDOS of elemental Se (Ref. 27) (Fig. 18) and acknowledged in the Se partial VDOS at a corresponding value of 4.6 meV (Fig. 19). With addition of Ge content, this contribution clearly loses intensity, in agreement with the loss of flexible modes for larger compositions.

B. Dielectric function

In order to gain additional details of the vibrational properties, we calculate the real and imaginary parts of the dielectric function, the latter being directly comparable to the infrared absorption spectra. During DFT simulation the total dipole moment $\mathbf{M}(t)$ can be evaluated²¹¹ and contributes via the Fourier transform of the dipole-dipole autocorrelation function to the absorption spectrum, using the linear response theory framework and the maximum entropy inversion method:²¹²

$$\alpha(\omega) = \frac{4\pi \tanh(\beta\hbar\omega/2)}{3\hbar c V n(\omega)} \int_0^\infty e^{-i\omega t} \langle \mathbf{M}(t) \mathbf{M}(0) \rangle dt, \quad (7)$$

where V is the volume, $\beta = 1/k_B T$, and $n(\omega)$ is the refractive index. Figure 20 shows the computed quantity $n(\omega)\alpha(\omega)$ which is nothing else than the imaginary part of the dielectric

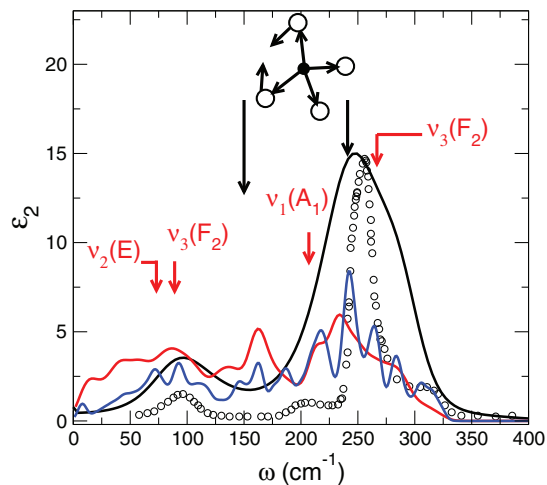


FIG. 20. (Color online) Computed imaginary part ε_2 of the dielectric function in GeSe_2 : Present calculation using the dipole-dipole autocorrelation function [Eq. (7), black curve], experimental measurement from IR absorption (Ref. 213) (circles), finite electric field method using either the PW (Ref. 216) (red curve) or the BLYP (Ref. 144) (blue curve) functional. Red arrows indicate the usual mode assignments (Refs. 209 and 217) and black arrows local modes extracted from the vibrational analysis of an isolated $\text{GeSe}_{4/2}$ tetrahedron (see text for details).

function ε_2 , i.e., the transverse response spectrum or infrared absorbance. The direct calculation for GeSe_2 using Eq. (7) is compared to experimental infrared data,²¹³ and to an alternative method²¹⁴ using a finite electric field in conjunction with the computation of coupling (dynamical Born charge²¹⁵) tensors based on the first derivative of the atomic forces with respect to the electrical field.^{144,216} When compared to experiment,²¹³ a clear improvement is obtained when dipole-dipole autocorrelation functions are used, instead of such alternative methods (Fig. 20). In fact, beyond positive methodological aspects [i.e., direct calculation of $\mathbf{M}(t)$ during the simulation^{207,218}], the present calculation marks substantial progress when compared to previous modeling of the dielectric function using either the Perdew-Wang²¹⁶ (PW) or the BLYP functional.¹⁴⁴ All typical spectral features^{209,213} of the IR spectrum of GeSe_2 are reproduced when using Eq. (7), i.e., a dominant line at 250 cm^{-1} , weak lines at 86 and 200 cm^{-1} , and a shoulder at about 300 cm^{-1} (arrows in Fig. 20). However, it should be noted that the calculated spectrum according to Eq. (7) has a much broader distribution when compared to experiment,²¹³ a situation which may arise from the small system size used. Furthermore, the lines are reproduced at a somewhat lower frequency ($\Delta\omega = 10 \text{ cm}^{-1}$). Other authors have suggested that excessive residual strain may also lead to a broadening of the spectra.²¹⁹ Nevertheless, the situation is much improved as previous simulations^{144,216} led only to a broad band between 0 and 350 m^{-1} while moderately acknowledging¹⁴⁴ the main peak at $\simeq 250 \text{ cm}^{-1}$ (Fig. 20). We are not aware of any systematic study of variation of the IR spectra with Ge content in $\text{Ge}_x\text{Se}_{1-x}$ glasses. However, based on our simulations, some general trends with Ge composition can be established from Fig. 21. The intensity and the frequency of the main peak change in

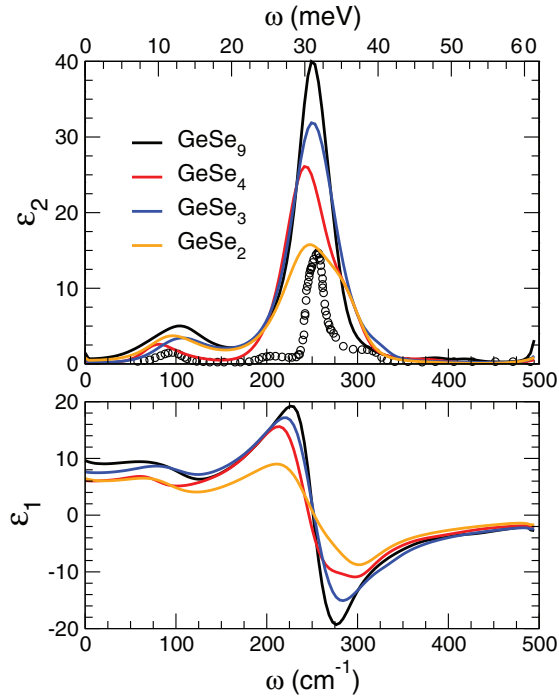


FIG. 21. (Color online) Computed imaginary ε_2 and real ε_1 parts of the dielectric function for the three investigated compositions of the $\text{Ge}_x\text{Se}_{1-x}$ glasses, compared to experimental measurements [circles (Ref. 213)].

a nonmonotonic fashion, the GeSe_4 compound displaying a lower line frequency (244 cm^{-1}) as compared to the other compositions (251 cm^{-1}), whereas its intensity decreases to $\varepsilon_2 = 26$. The secondary peak displays similar features. These results on selected compositions indicate that a study of IR absorbance across the stiffness transition would be highly desirable.

From the imaginary part ε_2 of the dielectric function, the real part ε_1 can be computed using the Kramers-Krönig equation (Fig. 21, bottom) and its changes followed with composition. This allows computation of the low-frequency (dc) limit ε_0 of the real part of the dielectric function ε_1 which displays a reasonable agreement with experimental data (Table VIII), certainly improved when compared to the previous simulations using the electric field method²¹⁶ ($\varepsilon_0 = 15.0$).

The identification of the different modes of ε_2 and their connection with Raman lines²⁰⁹ or vibrational densities of states^{27,100,127} have been quite extensively discussed in the literature. When compared to the simulated total and partial VDOSs (Figs. 18 and 19), one can associate the main peak of the IR spectrum (Fig. 21) with the Se stretching-mode vibration at 30 meV ($1\text{ meV} = 8.0655\text{ cm}^{-1}$). The overall decrease in

TABLE VIII. Calculated value of the dc dielectric permittivity ε_0 , and comparison with experimental data (Ref. 146).

	GeSe_9	GeSe_4	GeSe_3	GeSe_2	Ref.
ε_0	9.62	6.07	7.61	6.46	
	6.52	7.21	7.17	7.22	146

intensity of this peak closely follows the one found for ε_2 with a minimum intensity at the stoichiometric GeSe_2 . Correlations between the secondary peak of ε_2 at 86 cm^{-1} and a typical vibration frequency in the VDOS are less obvious, as it is for the other typical lines of the dielectric functions (200 and 300 cm^{-1}).

To gain additional insight and connect local vibrations with the typical frequencies obtained in the absorption spectrum (Fig. 21), we have used our electronic DFT scheme¹³⁸ to determine from an exact diagonalization of the Hessian matrix the vibrational eigenmodes and eigenvectors of an isolated $\text{GeSe}_{4/2}$ tetrahedron. There is some controversy around the mode assignment of the typical lines.^{96,100,168,209} From our frequency analysis and a visual inspection of the atomic motion, we find that the lines at 71 and 89 cm^{-1} are indeed^{168,209} associated with the identified E mode of frequency ν_2 , consisting of bending motion inside the tetrahedra. But in contrast with Ref. 209, we find that the A_1 stretching mode is weakly coupled to bending motions for two other frequencies at 151 cm^{-1} (low amplitude) and 241 cm^{-1} (large amplitude, i.e., the main peak in Fig. 20), and may both contribute to the experimental assignment^{100,209} of 200 cm^{-1} . Finally, modes found at the upper tail of the main line (260 and 272 cm^{-1}) consist in the reported stretch-antistretch F_2 mode. These modes are clearly absent for the nonstoichiometric compositions (Fig. 21), given the absence of this high-frequency tail for GeSe_9 , GeSe_4 , and GeSe_3 .

VIII. SUMMARY AND CONCLUSION

Glasses belonging to the $\text{Ge}_x\text{Se}_{1-x}$ family not only display a variety of structural features but also represent the archetypal system that serves for the detection of flexible to rigid transitions.^{21,22} The understanding of their structural, vibrational, thermal, and electronic properties is an important issue given that many optoelectronic applications using additives in ternary or multicomponent systems involve Ge and Se atoms as major alloying elements. Regarding structure, chains of Se atoms progressively cross-link with the addition of $\text{GeSe}_{4/2}$ tetrahedra, leading to a fully three-dimensional network that can be characterized using various experimental and theoretical tools. However, this simple picture not only fails to describe most of the nonmonotonic compositional trends of physicochemical properties, it also cannot account for an atomic-scale picture of the intermediate phase. In the present contribution we have used recently optimized^{138,141–144,220} first-principles molecular dynamics simulations to investigate in detail the effect of Ge composition on various properties by focusing on four target compositions GeSe_9 , GeSe_4 , GeSe_3 , and GeSe_2 . An additional recently investigated composition⁵¹ has also been used (Ge_2Se_3) in the analysis and the discussion. All these compositions span the previously determined elastic phases⁵⁰ characterized by rigidity theory: a flexible Se-rich phase which contains local deformation modes, a Ge-rich phase which is stressed rigid and locked by an important bond density, and a compositional interval (the intermediate phase) in which glasses seem to adapt in order to lower the compositionally induced stress. Attempts to understand these

features from molecular simulations have been reported only recently.²²¹

Regarding structural properties, our first-principles model appears to reproduce with great accuracy the available neutron diffraction results in both real and reciprocal space. The FSDP in the measured total structure factor at $\simeq 1 \text{ \AA}^{-1}$ is obtained and can also be investigated with varying composition in relevant partials focusing either on the topological [$S_{NN}(k)$] or on the chemical long-range [$S_{CC}(k)$] correlations. In real space, while the main structural $\text{GeSe}_{4/2}$ motif is found to connect with Se chains, we have determined all possible structural information that can be gathered from FPMD: coordination numbers, neighbor distributions, bond angle distributions. These show that the octet ($8 - N$) rule nearly holds for Se-rich glasses but then the results start to deviate as more and more miscoordinated species (Ge^{III} , Ge^{V} , Se^{III}) appear. Still, the majority of Se and Ge atoms are found to be twofold and fourfold coordinated, respectively. Similarly, the way these species connect together via the three available bonding types (Se-Se, Ge-Se, and Ge-Ge) has been characterized and its variation followed with composition. Among these, we find that the fraction of homopolar Ge-Ge bonds starts to increase at the upper boundary of the intermediate phase (GeSe_3), in line with similar findings on a parent system [As-Se (Ref. 154)]. The medium-range order has also been determined through a ring analysis which shows a nonmonotonic increase for small rings (fourfold-ring edge-sharing structures and also sixfold rings) across the stiffness transitions and the IP, while also exhibiting interesting ring correlations that can be entirely characterized using a quantitative ring analysis code.¹⁶⁰ The impact of Ge-Ge homopolar bonds is clearly visible in the ring statistics, which show that these connections occur in both even- and odd-membered rings and are particularly numerous in large-ring structures.

Having such precise atomic-scale trajectories in hand, one is also in a position to check the validity of simple models that have been proposed for amorphous Ge-Se networks. We have shown that the simple outrigger raft model proposed by Phillips and co-workers¹⁶⁸ (a model based on four-, five-, and sixfold rings with some homopolar Se-Se bonds) does not allow description of the structure of amorphous GeSe_2 . Instead, we find this ring structure to contain both homopolar Ge-Ge and Se-Se bonds but also rings of larger

sizes. Furthermore, the internal structure of each of these rings is determined from the fraction of homopolar versus heteropolar bonds, and appears to depend substantially on Ge composition. We also investigate the validity of simple pair models (random covalent network, chemically ordered network, clustered, chain-crossing, etc.) and show that none of them can reproduce the computed bond statistics that is extracted from the simulation and which takes into account the possibility of coordination defects. We have analyzed the trajectories from recently developed MD-based constraint counting algorithms¹⁸⁷ and have found that stressed rigid compositions (GeSe_2 and Ge_2Se_3) will have a rather important fraction (17%–21%) of their bond-bending (angular) interactions broken in order to accommodate the stress induced by the growing presence of the cross-linking Ge atoms. These findings actually cannot be recovered from simple constraint counting and represent therefore an interesting insight into the realistic atomic-scale behavior of rigidity.

What are the broader perspectives of the present work? Obviously, given the chosen system size (120 atoms) one can select only a few target compositions in the Ge-Se binary system. One is therefore not in a position to track the onset of rigidity and stress in these glasses, and particularly across the IP compositions. It would be interesting to investigate larger system sizes with such methods.¹⁵⁶ It would allow extending the present study by performing an analysis of structural, electronic, and vibrational properties within smaller compositional intervals. It would also permit better insight into the dynamics of glass-forming Ge-Se mixtures, and eventually the detection of anomalies associated with the intermediate phase, as in the parent As-Se system.¹⁵⁴

ACKNOWLEDGMENTS

The authors thank C. Bichara, P. Boolchand, S. Boshle, K. Gunasekera, G. G. Naumis, A. Pasquarello, J. C. Phillips, P. Simon, T. Rouxel, D. De Sousa-Meneses, and R. Vuilleumier for useful and stimulating discussions. L. Giacomazzi is acknowledged for sharing his data for Fig. 20. Support from Agence Nationale de la Recherche (ANR) (Grant No. 09-BLAN-0109-01) is gratefully acknowledged. GENCI (Grand Equipement National de Calcul Intensif) is acknowledged for supercomputing access.

*mmi@lptl.jussieu.fr

¹K. Shimawa, A. Kolobov, and S. R. Elliott, *Adv. Phys.* **44**, 475 (1995).

²M. N. Kozicki, M. Mitkova, J. Zhu, and M. Park, *Microelectron. Eng.* **63**, 155 (2002).

³A. Kolobov and S. R. Elliott, *Adv. Phys.* **40**, 625 (1991).

⁴J. Troles, V. Shiryaev, M. Churbanov, P. Houizot, L. Brilland, F. Desevedavy, F. Charpentier, T. Pain, G. Snopatin, and J. L. Adam, *Opt. Mater.* **32**, 212 (2009).

⁵J. T. Gopinath, M. Soljaèiae, E. P. Ippen, V. N. Fuflyigin, W. A. King, and M. Shurgalin, *J. Appl. Phys.* **96**, 6931 (2004).

⁶J. Keirsse, C. Boussard-Plénel, O. Loréal, O. Sire, B. Bureau, P. Leroyer, B. Turlin, and J. Lucas, *J. Non-Cryst. Solids* **326–327**, 430 (2003).

⁷A. B. Seddon and M. J. Laine, *J. Non-Cryst. Solids* **213–214**, 168 (1997).

⁸T. Kohoutek, T. Wagner, J. Orava, M. Krbal, J. Ilavsky, M. Vlcek, and M. Frumar, *J. Non-Cryst. Solids* **354**, 529 (2008).

⁹W. J. Bresser, P. Boolchand, P. Suranyi, and J. P. de Neufville, *Phys. Rev. Lett.* **46**, 1689 (1981).

¹⁰P. Boolchand, J. Grothaus, W. J. Bresser, and P. Suranyi, *Phys. Rev. B* **25**, 2975 (1982).

- ¹¹K. Shimakawa, S. Inami, T. Kato, and S. R. Elliott, *Phys. Rev. B* **46**, 10062 (1992).
- ¹²C. R. Schardt, P. Lucas, A. Doraiswamy, P. Jivaganont, and J. H. Simmons, *J. Non-Cryst. Solids* **351**, 1653 (2005).
- ¹³Y. Gueguen, J. Ch. Sangleboeuf, V. Keryvin, E. Lépine, Z. Yang, T. Rouxel, C. Point, B. Bureau, X.-H. Zhang, and P. Lucas, *Phys. Rev. B* **82**, 134114 (2010).
- ¹⁴P. Lucas, E. A. King, A. Doraiswamy, and P. Jivaganont, *Phys. Rev. B* **71**, 104207 (2005).
- ¹⁵B. Singh, S. Rajagopalan, P. K. Bhat, D. K. Pandya, and K. L. Chopra, *J. Non-Cryst. Solids* **35–36**, 1053 (1980).
- ¹⁶B. Singh, S. Rajagopalan, and K. L. Chopra, *J. Appl. Phys.* **51**, 1768 (1980).
- ¹⁷M. Jin, P. Chen, P. Boolchand, T. Rajagopalan, K. L. Chopra, K. Starbova, and N. Starbov, *Phys. Rev. B* **78**, 214201 (2008).
- ¹⁸D. D. Jeong, H. Lim, G. H. Park, C. S. Hwang, S. Lee, and B. K. Cheong, *J. Appl. Phys.* **111**, 102807 (2012).
- ¹⁹J. L. Lagrange, *Mécanique Analytique* (Paris, 1788).
- ²⁰J. C. Maxwell, *Philos. Mag.* **27**, 294 (1864).
- ²¹J. C. Phillips, *J. Non-Cryst. Solids* **34**, 153 (1979).
- ²²M. F. Thorpe, *J. Non-Cryst. Solids* **57**, 355 (1983).
- ²³H. He and M. F. Thorpe, *Phys. Rev. Lett.* **54**, 2107 (1985).
- ²⁴M. Micoulaut and J. C. Phillips, *Phys. Rev. B* **67**, 104204 (2003).
- ²⁵M. F. Thorpe, D. J. Jacobs, M. V. Chubynsky, and J. C. Phillips, *J. Non-Cryst. Solids* **266–269**, 859 (2000).
- ²⁶*Phase Transitions and Self-organization in Electronic and Molecular Networks*, edited by M. F. Thorpe and J. C. Phillips (Kluwer Academic/Plenum, New York, 2001).
- ²⁷W. A. Kamitakahara, R. L. Cappelletti, P. Boolchand, B. Halfpap, F. Gompf, D. A. Neumann, and H. Mutka, *Phys. Rev. B* **44**, 94 (1991).
- ²⁸A. N. Sreeram, A. K. Varshneya, and D. R. Swiler, *J. Non-Cryst. Solids* **128**, 294 (1991).
- ²⁹P. Boolchand, W. J. Bresser, M. Zhang, Y. Wu, J. Wells, and R. N. Enzweiler, *J. Non-Cryst. Solids* **182**, 143 (1995).
- ³⁰M. Tatsumisago, B. L. Halfpap, J. L. Green, S. M. Lindsay, and C. A. Angell, *Phys. Rev. Lett.* **64**, 1549 (1990).
- ³¹S. Asokan, M. V. N. Prasad, G. Parthasarathy, and E. S. R. Gopal, *Phys. Rev. Lett.* **62**, 808 (1989).
- ³²J. C. Phillips, *Phys. Rev. B* **28**, 7038 (1983).
- ³³M. T. Clavaguera-Mora, M. D. Barò, S. Surinach, J. Saurina, and N. Clavaguera, *J. Non-Cryst. Solids* **131–133**, 479 (1991).
- ³⁴U. Senapati and A. K. Varshnaya, *J. Non-Cryst. Solids* **185**, 289 (1995).
- ³⁵R. Golovchak, A. Kozdras, S. Kozyukhin, and O. Shpotyuk, *Nucl. Instrum. Methods Phys. Res. B* **267**, 2958 (2009).
- ³⁶J. M. Saiter, A. Hamou, and C. Vautier, *J. Non-Cryst. Solids* **172–174**, 580 (1994).
- ³⁷J. Y. Duquesne and G. Bellassa, *J. Phys. Colloq.* **46**, C10 (1985).
- ³⁸J.-P. Guin, T. Rouxel, V. Keryvin, J.-Ch. Sangleboeuf, I. Serre, and J. Lucas, *J. Non-Cryst. Solids* **298**, 260 (2002).
- ³⁹G. Yang, B. Bureau, T. Rouxel, Y. Gueguen, O. Gulbiten, C. Roiland, E. Soignard, J. L. Yarger, J. Troles, J.-Ch. Sangleboeuf, and P. Lucas, *Phys. Rev. B* **82**, 195206 (2010).
- ⁴⁰Y. Tsuchiya, *J. Non-Cryst. Solids* **122**, 205 (1990).
- ⁴¹J. Gump, I. Finkler, H. Xia, R. Sooryakumar, W. J. Bresser, and P. Boolchand, *Phys. Rev. Lett.* **92**, 245501 (2004).
- ⁴²A. Laugier, G. Chaussemy, and J. Fornazero, *J. Non-Cryst. Solids* **23**, 419 (1977).
- ⁴³S. Stølen, T. Grande, H.-B. Johnsen, *Phys. Chem. Chem. Phys.* **4**, 3396 (2002).
- ⁴⁴Y. Gueguen, T. Rouxel, P. Gadaud, C. Bernard, V. Keryvin, and J.-Ch. Sangleboeuf, *Phys. Rev. B* **84**, 064201 (2011).
- ⁴⁵X. Feng, W. J. Bresser, and P. Boolchand, *Phys. Rev. Lett.* **78**, 4422 (1997).
- ⁴⁶D. Selvenathan, W. Bresser, and P. Boolchand, *Solid State Commun.* **111**, 619 (1999).
- ⁴⁷D. Selvenathan, W. J. Bresser, and P. Boolchand, *Phys. Rev. B* **61**, 15061 (2000).
- ⁴⁸G. Chen, F. Inam, and D. A. Drabold, *J. Appl. Phys.* **97**, 131901 (2010).
- ⁴⁹P. Boolchand, P. Chen, M. Jin, B. Goodman, and W. J. Bresser, *Physica B* **389**, 18 (2007).
- ⁵⁰S. Bhosle, K. Gunasekera, P. Chen, P. Boolchand, M. Micoulaut, and C. Massobrio, *Solid State Commun.* **151**, 1851 (2011).
- ⁵¹S. Le Roux, A. Bouzid, M. Boero, and C. Massobrio, *Phys. Rev. B* **86**, 224201 (2012).
- ⁵²S. Chakravarty, D. G. Georgiev, P. Boolchand, and M. Micoulaut, *J. Phys.: Condens. Matter* **17**, L1 (2005).
- ⁵³D. G. Georgiev, P. Boolchand, and M. Micoulaut, *J. Optoelectron. Adv. Mater.* **4**, 823 (2002).
- ⁵⁴F. Wang, S. Mamedov, P. Boolchand, B. Goodman, and M. Chandrasekhar, *Phys. Rev. B* **71**, 174201 (2005).
- ⁵⁵C. Bourgel, M. Micoulaut, M. Malki, and P. Simon, *Phys. Rev. B* **79**, 024201 (2009).
- ⁵⁶R. Rompicharla, D. I. Novita, P. Chen, P. Boolchand, M. Micoulaut, and W. Huff, *J. Phys.: Condens. Matter* **20**, 202101 (2008).
- ⁵⁷M. Micoulaut, M. Malki, P. Simon, and A. Canizares, *Philos. Mag.* **85**, 3357 (2005).
- ⁵⁸F. Wang, P. Boolchand, K. Jackson, and M. Micoulaut, *J. Phys.: Condens. Matter* **19**, 226201 (2007).
- ⁵⁹G. Sreevidya Varma, M. S. R. N. Kiran, D. V. S. Muthu, U. Ramamurty, A. K. Sood, and S. Asokan, *J. Non-Cryst. Solids* **358**, 3103 (2012).
- ⁶⁰R. G. Srinivasa, A. Arunbabu, and S. Asokan, *J. Solid State Chem.* **184**, 3345 (2011).
- ⁶¹B. J. Madhu, H. S. Jayanna, and S. Asokan, *Eur. Phys. J. B* **71**, 21 (2009).
- ⁶²P. Chen, C. Holbrook, P. Boolchand, D. G. Georgiev, K. A. Jackson, and M. Micoulaut, *Phys. Rev. B* **78**, 224208 (2008).
- ⁶³J. C. Phillips, *Phys. Rev. Lett.* **88**, 216401 (2002).
- ⁶⁴A. J. Rader, B. Hespeneide, L. Kuhn, and M. F. Thorpe, *Proc. Natl. Acad. Sci. USA* **99**, 3540 (2002).
- ⁶⁵D. J. Jacobs, A. J. Rader, L. A. Kuhn, and M. F. Thorpe, *Proteins* **44**, 150 (2001).
- ⁶⁶M. Micoulaut and M. Bauchy, *Phys. Status Solidi B* **250**, 976 (2013).
- ⁶⁷*Rigidity and Boolchand Phases in Nanomaterials*, edited by M. Micoulaut and M. Popescu (INOE Publishing House, Bucarest, 2009).
- ⁶⁸S. Bhosle, K. Gunasekera, P. Boolchand, and M. Micoulaut, *Int. J. Appl. Glass Science* **3**, 205 (2012).
- ⁶⁹S. Bhosle, K. Gunasekera, P. Boolchand, and M. Micoulaut, *Int. J. Appl. Glass Science* **3**, 189 (2012).
- ⁷⁰D. I. Novita and P. Boolchand, *Phys. Rev. B* **76**, 184205 (2007).
- ⁷¹P. Chen, P. Boolchand, and D. G. Georgiev, *J. Phys.: Condens. Matter* **22**, 065104 (2010).

- ⁷²R. Golovchak, H. Jain, O. Shpotyuk, A. Kozdras, A. Saiter, and J.-M. Saiter, *Phys. Rev. B* **78**, 014202 (2008).
- ⁷³M. Micoulaut, *Phys. Rev. B* **74**, 184208 (2006).
- ⁷⁴J. Barré, A. R. Bishop, T. Lookman, and A. Saxena, *Phys. Rev. Lett.* **94**, 208701 (2005).
- ⁷⁵M. V. Chubynsky, M. A. Brière, and N. Mousseau, *Phys. Rev. E* **74**, 016116 (2006).
- ⁷⁶K. Maruyama, M. Inui, S. Takeda, S. Tamaki, and Y. Kawakita, *Physica B* **213–214**, 558 (1995).
- ⁷⁷K. Maruyama, H. Ebata, S. Suzuki, M. Misawa, S. Takeda, S. Tamaki, and Y. Kawakita, *J. Non-Cryst. Solids* **250–252**, 483 (1999).
- ⁷⁸N. Ramesh Rao, P. S. R. Krishna, S. Basu, B. A. Dasannacharya, K. S. Sangunni, and E. S. R. Gopal, *J. Non-Cryst. Solids* **240**, 221 (1998).
- ⁷⁹I. T. Penfold and P. S. Salmon, *J. Phys.: Condens. Matter* **2**, SA233 (1990).
- ⁸⁰I. T. Penfold and P. S. Salmon, *Phys. Rev. Lett.* **67**, 97 (1991).
- ⁸¹I. Petri, P. S. Salmon, and H. E. Fischer, *J. Phys.: Condens. Matter* **11**, 7051 (1999).
- ⁸²I. Petri and P. S. Salmon, *Phys. Chem. Glasses* **43C**, 185 (2002).
- ⁸³P. S. Salmon, *J. Non-Cryst. Solids* **353**, 2959 (2007).
- ⁸⁴E. Bychkov, C. J. Benmore, and D. L. Price, *Phys. Rev. B* **72**, 172107 (2005).
- ⁸⁵J. C. Malaurent and J. Dixmier, *J. Non-Cryst. Solids* **35–36**, 1227 (1980).
- ⁸⁶M. M. Hafiz, F. H. Hammad, and N. A. El-Kabany, *Physica B* **183**, 392 (1993).
- ⁸⁷W. A. Crichton, M. Mezouar, T. Grande, S. Stølen, and A. Grzechnik, *Nature (London)* **414**, 622 (2001).
- ⁸⁸Y. Wang, E. Ohata, S. Hosokawa, M. Sakurai, and E. Matsubara, *J. Non-Cryst. Solids* **337**, 54 (2004).
- ⁸⁹P. H. Fuoss and A. Fischer-Colbrie, *Phys. Rev. B* **38**, 1875 (1988).
- ⁹⁰M. T. M. Shatnawi, C. L. Farrow, P. Chen, P. Boolchand, A. Sartbaeva, M. F. Thorpe, and S. J. L. Billinge, *Phys. Rev. B* **77**, 094134 (2008).
- ⁹¹C. Peyroutou, S. Peytavin, M. Ribes, and H. Dexpert, *J. Solid State Chem.* **82**, 78 (1989).
- ⁹²S. J. Gurman, J. Choi, and E. A. Davis, *J. Non-Cryst. Solids* **227–230**, 833 (1998); J. Choi, S. J. Gurman, and E. A. Davis, *ibid.* **297**, 156 (2002).
- ⁹³W. Zhou, M. Paesler, and D. E. Sayers, *Phys. Rev. B* **43**, 2315 (1991).
- ⁹⁴E. Gulbrandsen, H. B. Johnsen, M. Endregaard, T. Grande, and S. Stølen, *J. Solid State Chem.* **145**, 253 (1999).
- ⁹⁵P. Tronc, M. Bensoussan, A. Brenac, and C. Sebenne, *Phys. Rev. B* **8**, 5947 (1973).
- ⁹⁶S. Sugai, *Phys. Rev. B* **35**, 1345 (1987).
- ⁹⁷S. Onari, K. Matsuichi, and T. Arai, *J. Non-Cryst. Solids* **77–78**, 1121 (1985).
- ⁹⁸L. F. Gladden, S. R. Elliott, R. N. Sinclair, and A. C. Wright, *J. Non-Cryst. Solids* **106**, 120 (1988).
- ⁹⁹L. Orsingher, G. Baldi, A. Fontana, L. E. Bove, T. Unruh, A. Orecchini, C. Petrillo, N. Violini, and F. Sacchetti, *Phys. Rev. B* **82**, 115201 (2010).
- ¹⁰⁰U. Walter, D. L. Price, S. Susman, and K. J. Volin, *Phys. Rev. B* **37**, 4232 (1988).
- ¹⁰¹S. Hosokawa, Y. Wang, M. Sakurai, J. F. Bérrar, W. C. Pilgrim, and K. Murase, *Nucl. Instrum. Methods Phys. Res. B* **199**, 165 (2003).
- ¹⁰²S. Hosokawa, I. Oh, M. Sakurai, W.-C. Pilgrim, N. Boudet, J.-F. Bérrar, and S. Kohara, *Phys. Rev. B* **84**, 014201 (2011).
- ¹⁰³W. Bresser, P. Boolchand, and P. Suranyi, *Phys. Rev. Lett.* **56**, 2493 (1986).
- ¹⁰⁴P. Boolchand, J. Grothaus, M. Tenhover, M. A. Hazle, and R. K. Grasselli, *Phys. Rev. B* **33**, 5421 (1986).
- ¹⁰⁵B. Bureau, J. Troles, M. Le Floch, P. Guénot, F. Smektala, and J. Lucas, *J. Non-Cryst. Solids* **319**, 145 (2003).
- ¹⁰⁶P. Lucas, E. A. King, O. Gulbitten, J. L. Yarger, E. Soignard, and B. Bureau, *Phys. Rev. B* **80**, 214114 (2009).
- ¹⁰⁷S. Sen and Z. Gan, *J. Non-Cryst. Solids* **356**, 1519 (2010).
- ¹⁰⁸E. L. Gjersing, S. Sen, and R. E. Youngman, *Phys. Rev. B* **82**, 014203 (2010).
- ¹⁰⁹P. S. Salmon and I. Petri, *J. Phys.: Condens. Matter* **15**, S1509 (2003).
- ¹¹⁰I. Petri, P. S. Salmon, and H. E. Fischer, *Phys. Rev. Lett.* **84**, 2413 (2000).
- ¹¹¹M. Durandurdu and D. A. Drabold, *Phys. Rev. B* **65**, 104208 (2002).
- ¹¹²A. A. Andreev, B. T. Melekh, and T. Turganov, *Sov. Phys. Solid State* **18**, 141 (1976).
- ¹¹³K. D. Machado, J. C. de Lima, C. E. M. Campos, A. A. M. Gasperini, S. M. de Souza, C. E. Maurmann, T. A. Grandi, and P. S. Pizani, *Solid State Commun.* **133**, 411 (2005).
- ¹¹⁴A. H. Moharram and A. M. Abdel-Basset, *Physica B* **405**, 4240 (2010).
- ¹¹⁵K. D. Machado, J. C. de Lima, C. E. M. Campos, T. A. Grandi, and P. S. Pizani, *J. Chem. Phys.* **120**, 329 (2004).
- ¹¹⁶H. Iyetomi, P. Vashishta, and R. K. Kalia, *Solid State Ion.* **32–33**, 954 (1989).
- ¹¹⁷P. Vashishta, R. K. Kalia, G. A. Antonio, and I. Ebbsjö, *Phys. Rev. Lett.* **62**, 1651 (1989).
- ¹¹⁸P. Vashishta, R. K. Kalia, G. A. Antonio, J. P. Rino, H. Iyetomi, and I. Ebbsjö, *Solid State Ion.* **40–41**, 175 (1990).
- ¹¹⁹H. Iyetomi, P. Vashishta, and R. K. Kalia, *Phys. Rev. B* **43**, 1726 (1991).
- ¹²⁰H. Iyetomi and P. Vashishta, *Phys. Rev. B* **47**, 3063 (1993).
- ¹²¹P. Vashishta, R. K. Kalia, and I. Ebbsjö, *Solid State Ion.* **32–33**, 872 (1989).
- ¹²²J. C. Mauro and A. K. Varshneya, *J. Am. Ceram. Soc.* **89**, 1091 (2005).
- ¹²³J. C. Mauro and A. K. Varshneya, *J. Am. Ceram. Soc.* **90**, 192 (2007).
- ¹²⁴B. K. Sharma and M. Wilson, *Phys. Rev. B* **73**, 060201 (2006).
- ¹²⁵M. Wilson, B. K. Sharma, and C. Massobrio, *J. Chem. Phys.* **128**, 244505 (2008).
- ¹²⁶M. Cobb, D. A. Drabold, and R. L. Cappelletti, *Phys. Rev. B* **54**, 12162 (1996).
- ¹²⁷R. L. Cappelletti, M. Cobb, D. A. Drabold, and W. A. Kamitakahara, *Phys. Rev. B* **52**, 9133 (1995).
- ¹²⁸D. N. Tafen and D. A. Drabold, *Phys. Rev. B* **71**, 054206 (2005).
- ¹²⁹F. Inam, D. A. Drabold, M. Shatnawi, D. Tafen, P. Chen, and S. Billinge, *J. Phys.: Condens. Matter* **19**, 455206 (2007).
- ¹³⁰K. Hachiya, *J. Non-Cryst. Solids* **291**, 160 (2001).
- ¹³¹K. A. Jackson, S. Srinivas, J. Kortus, and M. Pederson, *Phys. Rev. B* **65**, 214201 (2002).
- ¹³²K. Jackson, A. Briley, S. Grossman, D. V. Porezag, and M. R. Pederson, *Phys. Rev. B* **60**, R14985 (1999).
- ¹³³C. Massobrio, F. H. M. van Roon, A. Pasquarello, and S. W. De Leeuw, *J. Phys.: Condens. Matter* **12**, L697 (2000).

- ¹³⁴C. Massobrio, A. Pasquarello, and R. Car, *Phys. Rev. Lett.* **80**, 2342 (1998).
- ¹³⁵C. Massobrio, A. Pasquarello, and R. Car, *Phys. Rev. B* **64**, 144205 (2001).
- ¹³⁶C. Massobrio and A. Pasquarello, *Phys. Rev. B* **77**, 144207 (2008).
- ¹³⁷C. Massobrio, A. Pasquarello, and R. Car, *J. Am. Chem. Soc.* **121**, 2943 (1999).
- ¹³⁸M. Micoulaut, R. Vuilleumier, and C. Massobrio, *Phys. Rev. B* **79**, 214205 (2009).
- ¹³⁹A. D. Becke, *Phys. Rev. A* **38**, 3098 (1988).
- ¹⁴⁰C. Lee, W. Yang, and R. G. Parr, *Phys. Rev. B* **37**, 785 (1988).
- ¹⁴¹M. Micoulaut and C. Massobrio, *J. Optoelectr. Adv. Mater.* **12**, 1897 (2009).
- ¹⁴²C. Massobrio, M. Micoulaut, and P. S. Salmon, *Solid State Sci.* **12**, 199 (2010).
- ¹⁴³M. Bauchy, M. Micoulaut, M. Celino, S. Le Roux, M. Boero, and C. Massobrio, *Phys. Rev. B* **84**, 054201 (2011).
- ¹⁴⁴L. Giacomazzi, C. Massobrio, and A. Pasquarello, *J. Phys.: Condens. Matter* **23**, 295401 (2011).
- ¹⁴⁵M. Kibalchenko, J. R. Yates, C. Massobrio, and A. Pasquarello, *Phys. Rev. B* **82**, 020202 (2010).
- ¹⁴⁶A. Feltz, H. Aust, and A. Blayer, *J. Non-Cryst. Solids* **55**, 179 (1983).
- ¹⁴⁷R. Car and M. Parrinello, *Phys. Rev. Lett.* **55**, 2471 (1985).
- ¹⁴⁸H. E. Fischer, A. C. Barnes, and P. S. Salmon, *Rep. Prog. Phys.* **69**, 233 (2006).
- ¹⁴⁹P. S. Salmon, R. A. Martin, P. E. Mason, and G. Cuello, *Nature (London)* **435**, 75 (2005).
- ¹⁵⁰C. Massobrio and A. Pasquarello, *Phys. Rev. B* **75**, 014206 (2007).
- ¹⁵¹G. G. Naumis, *Phys. Rev. B* **73**, 172202 (2006).
- ¹⁵²M. Micoulaut, *Eur. Phys. J. B* **1**, 277 (1998).
- ¹⁵³We relate the position r of a peak in real space to the position k of a corresponding peak in Fourier space by using the relation $kr \approx 7.7$, which identifies the location of the first maximum of the spherical Bessel function $j_0(kr)$. See P. S. Salmon, *Proc. R. Soc. London, Ser. A* **445**, 351 (1994).
- ¹⁵⁴M. Bauchy, M. Micoulaut, M. Boero, and C. Massobrio, *Phys. Rev. Lett.* **110**, 165501 (2013).
- ¹⁵⁵D. G. Georgiev, P. Boolchand, and M. Micoulaut, *Phys. Rev. B* **62**, R9228 (2000).
- ¹⁵⁶M. Micoulaut, S. Le Roux, and C. Massobrio, *J. Chem. Phys.* **136**, 224504 (2012).
- ¹⁵⁷C. Massobrio, M. Celino, P. S. Salmon, R. A. Martin, M. Micoulaut, and A. Pasquarello, *Phys. Rev. B* **79**, 174201 (2009).
- ¹⁵⁸S. Mamedov, D. G. Georgiev, T. Qu, and P. Boolchand, *J. Phys.: Condens. Matter* **15**, S2397 (2003).
- ¹⁵⁹D. Caprion and H. R. Schober, *Phys. Rev. B* **62**, 3709 (2000).
- ¹⁶⁰S. Le Roux and P. Jund, *Comput. Mater. Sci.* **49**, 70 (2010); **50**, 1217 (2011).
- ¹⁶¹V. King, *Nature (London)* **213**, 1112 (1967).
- ¹⁶²D. S. Franzblau, *Phys. Rev. B* **44**, 4925 (1991).
- ¹⁶³X. Yuan and A. N. Cormack, *Comput. Mater. Sci.* **24**, 343 (2002).
- ¹⁶⁴M. Micoulaut, X. Yuan, and L. W. Hobbs, *J. Non-Cryst. Solids* **353**, 1951 (2007).
- ¹⁶⁵V. S. Minaev, S. P. Timoshenko, and V. V. Kalugin, *J. Optoelectron. Adv. Mater.* **7**, 1717 (2005).
- ¹⁶⁶F. Kirchoff, G. Kresse, and M. J. Gillan, *Phys. Rev. B* **57**, 10482 (1998).
- ¹⁶⁷M. Misawa and K. Suzuki, *J. Phys. Soc. Jpn.* **44**, 1612 (1978).
- ¹⁶⁸P. M. Bridenbaugh, G. P. Espinosa, J. E. Griffiths, J. C. Phillips, and J. P. Remeika, *Phys. Rev. B* **20**, 4140 (1979).
- ¹⁶⁹G. Dittmar and H. Schafer, *Acta Crystallogr.* **12**, 1188 (1976).
- ¹⁷⁰J. M. Peters and L. E. McNeil, *J. Non-Cryst. Solids* **139**, 231 (1992).
- ¹⁷¹P. Boolchand, J. Grothaus, and J. C. Phillips, *Solid State Commun.* **45**, 183 (1983).
- ¹⁷²P. H. Fuoss, P. Eisenberger, W. K. Warbuton, and A. Bienenstock, *Phys. Rev. Lett.* **46**, 1537 (1981).
- ¹⁷³F. L. Galeener, A. J. Leadbetter, and M. W. Stringfellow, *Phys. Rev. B* **27**, 1052 (1983).
- ¹⁷⁴L. Giacomazzi, P. Umari, and A. Pasquarello, *Phys. Rev. Lett.* **95**, 075505 (2005).
- ¹⁷⁵E. L. Gjersing, S. Sen, and B. Aitken, *J. Phys. Chem. C* **114**, 8601 (2010).
- ¹⁷⁶S. Le Roux and P. Jund, *J. Phys.: Condens. Matter* **19**, 196102 (2007).
- ¹⁷⁷S. Le Roux and P. Jund, *J. Non-Cryst. Solids* **355**, 1807 (2009).
- ¹⁷⁸S. R. Elliott, *The Physics of Amorphous Materials* (Longman, Harlow, 1990).
- ¹⁷⁹K. S. Liang, A. Bienenstock, and C. W. Bates, *Phys. Rev. B* **10**, 1528 (1974).
- ¹⁸⁰J. Dixmier and R. Mosseri, *J. Phys. Lett.* **41**, 5 (1980).
- ¹⁸¹R. M. White, *J. Non-Cryst. Solids* **16**, 387 (1974).
- ¹⁸²T. G. Edwards, S. Sen, and E. L. Gjersing, *J. Non-Cryst. Solids* **358**, 609 (2012).
- ¹⁸³B. Bureau, J. Troles, M. Le Floch, F. Smektala, and J. Lucas, *J. Non-Cryst. Solids* **326–327**, 58 (2003).
- ¹⁸⁴M. Micoulaut, *J. Optoelectron. Adv. Mater.* **10**, 3235 (2007).
- ¹⁸⁵Note that the displayed random distribution of trimers Se-Se-Se and Se-Se-Ge differs substantially from the one proposed in Ref. 175, as all possible connections and pathways of triplet production (Refs. 24 and 186) including random ring structures are taken into account.
- ¹⁸⁶M. Micoulaut, R. Kerner, and D. M. dos Santos-Loff, *J. Phys.: Condens. Matter* **7**, 8035 (1995).
- ¹⁸⁷M. Bauchy and M. Micoulaut, *J. Non-Cryst. Solids* **357**, 2530 (2011).
- ¹⁸⁸M. Micoulaut, J. Y. Raty, C. Otjacques, and C. Bichara, *Phys. Rev. B* **81**, 174206 (2010).
- ¹⁸⁹M. Bauchy and M. Micoulaut, *Phys. Rev. Lett.* **110**, 095501 (2013).
- ¹⁹⁰N. Mousseau and M. F. Thorpe, *Phys. Rev. B* **52**, 2660 (1995).
- ¹⁹¹K. Inoue, T. Katayama, K. Kawamoto, and K. Murase, *Phys. Rev. B* **35**, 7496 (1987).
- ¹⁹²E. Bergignat, G. Hollinger, H. Chermette, P. Pertosa, D. Lohez, M. Lannoo, and M. Bensoussan, *Phys. Rev. B* **37**, 4506 (1988).
- ¹⁹³R. Golovchak, O. Shpotyuk, S. Kozyukhin, A. Kovalskiy, A. C. Miller, and H. Jain, *J. Appl. Phys.* **105**, 103704 (2009).
- ¹⁹⁴S. G. Louie, *Phys. Rev. B* **26**, 5993 (1982).
- ¹⁹⁵W. Pollard, *J. Non-Cryst. Solids* **144**, 70 (1992).
- ¹⁹⁶M. Lannoo and M. Bensoussan, *Phys. Rev. B* **16**, 3546 (1977).
- ¹⁹⁷S. Hino, T. Kaharshi, and Y. Harada, *Solid State Commun.* **35**, 379 (1980).
- ¹⁹⁸S. Hosokawa, K. Nishihara, Y. Hari, M. Taniguchi, O. Matsuda, and K. Murase, *Phys. Rev. B* **47**, 15509 (1993).
- ¹⁹⁹M. Taniguchi, T. Kouchi, I. Ono, S. Hosokawa, M. Nakatake, H. Namatame, and K. Murase, *J. Electron Spectrosc. Relat. Phenom.* **78**, 507 (1996).

- ²⁰⁰A. Kumar, S. Goel, and S. K. Tripathi, *Phys. Rev. B* **38**, 13432 (1988).
- ²⁰¹J. Shirafuji, G. I. Kim, and Y. Inuishi, *Jpn. J. Appl. Phys.* **16**, 67 (1977).
- ²⁰²P. Klocek and L. Colombo, *J. Non-Cryst. Solids* **93**, 1 (1987).
- ²⁰³D. E. Aspnes, J. C. Phillips, K. L. Tai, and P. M. Bridenbaugh, *Phys. Rev. B* **23**, 816 (1981).
- ²⁰⁴D. Islam and R. L. Cappelletti, *Phys. Rev. B* **44**, 2516 (1991).
- ²⁰⁵D. A. Schmidt, R. Scipioni, and M. Boero, *J. Phys. Chem. A* **113**, 7725 (2009).
- ²⁰⁶B. G. Johnson, P. M. W. Gill, and J. A. Pople, *J. Chem. Phys.* **98**, 5612 (1998).
- ²⁰⁷R. J. Nemanich, F. L. Galeener, J. C. Mikkelsen, G. A. N. Connel, G. Etherington, A. C. Wright, and R. N. Sinclair, *Physica B+C* **117–118**, 989 (1983).
- ²⁰⁸P. N. Sen and M. F. Thorpe, *Phys. Rev. B* **15**, 4030 (1977).
- ²⁰⁹N. Kumagai, J. Shirafuji, and Y. Inuishi, *J. Phys. Soc. Jpn.* **42**, 1262 (1977).
- ²¹⁰Y. Cai and M. F. Thorpe, *Phys. Rev. B* **40**, 10535 (1989).
- ²¹¹P. L. Silvestrelli, M. Bernasconi, and M. Parrinello, *Chem. Phys. Lett.* **277**, 478 (1997).
- ²¹²R. N. Silver, D. S. Sivia, and J. E. Gubernatis, *Phys. Rev. B* **41**, 2380 (1990).
- ²¹³G. Lucovsky, R. J. Nemanich, S. A. Solin, and R. C. Keezer, *Solid State Commun.* **17**, 1567 (1975).
- ²¹⁴P. Umari and A. Pasquarello, *Phys. Rev. Lett.* **89**, 157602 (2002).
- ²¹⁵R. Resta, *Rev. Mod. Phys.* **66**, 899 (1994).
- ²¹⁶L. Giacomazzi, C. Massobrio, and A. Pasquarello, *Phys. Rev. B* **75**, 174207 (2007).
- ²¹⁷G. Herzberg, *Infrared and Raman Spectra of Polyatomic Molecules* (Van Nostrand, New York, 1945).
- ²¹⁸M. Boero, K. Terakura, T. Ikeshoji, C. C. Liew, and M. Parrinello, *J. Chem. Phys.* **115**, 2219 (2001).
- ²¹⁹P. Umari and A. Pasquarello, *Diamond Relat. Mater.* **14**, 1255 (2005).
- ²²⁰O. Dietz, U. Kuhl, H.-J. Stöckmann, N. M. Makarov, and F. M. Izraelev, *Phys. Rev. B* **83**, 134203 (2011).
- ²²¹F. Inam, G. Chen, D. N. Tafen, and D. A. Drabold, *Phys. Status Solidi B* **246**, 1849 (2009).